Predicting the strain-hardening behaviour of polyethylene fibre reinforced engineered cementitious composites accounting for fibre-matrix interaction

Binrong Zhu[a,b], Jinlong Pan[a,*], Mingzhong Zhang[b,**], Christopher K.Y. Leung[c]

[a] *Key Laboratory of Concrete and Prestressed Concrete Structures of Ministry of Education, School of Civil Engineering, Southeast University, Nanjing, 211189, China*

[b] *Department of Civil, Environmental and Geomatic Engineering, University College London, London, WC1E 6BT, UK*

[c] *Department of Civil and Environmental Engineering, The Hong Kong University of Science and Technology, Clear Water Bay, Kowloon, Hong Kong, China*

Abstract: Mechanical properties of engineered cementitious composites (ECC) are highly dependent on the pore structural characteristics and fibre-matrix interaction. The relationship between them has not been extensively explored. This paper proposes a practical micromechanical analytical model accounting for pore structure characteristics and crack-bridging properties to predict the strain-hardening and multiple microcracking behaviour of ECC. Using polyethylene fibre reinforced ECC (PE-ECC) as an example, Monte Carlo simulations were undertaken to investigate the tensile behaviour in terms of crack strength, fibre bridging strength and uniaxial tensile properties against heterogeneity of material property, which were validated with experimental data. A parametric study was then conducted to estimate the effects of fibre-matrix bond and fibre properties on stress-strain relationship and microcracking features of PE-ECC. Results indicate that the tensile properties of PE-ECC can be reasonably predicted. Under constant fibre dosages, the tensile ductility of PE-ECC is dominated by interfacial bond, followed by fibre location, orientation and diameter. Such insights are helpful to the design of ECC composites for practical applications.

Keywords: Strain-hardening cementitious composites; Micromechanics-based design; Fibre pull-out; Fibre-matrix bond; Tensile behaviour; Microstructure

* Corresponding author. E-mail address: cejlpan@seu.edu.cn (J. Pan).

** Corresponding author. E-mail address: mingzhong.zhang@ucl.ac.uk (M. Zhang).

Nomenclature

$\bar{C}$	normalised crack radius at the peak crack-bridging displacement	r, q	shape parameters in $p(\theta)$
c	pore size bridged by fibres during crack growth	u	pull-out displacement under single fibre pull-out test
c_p	nominal initial pore size without fibre across it	u_0	pull-out displacement at peak force under single fibre pull-out test
c_n	nominal initial pore size for the n^{th} section	V_f	volume fraction of fibre
d_f	fibre diameter	V_{fn}	local fibre volume fraction for the n^{th} section
E_c	composite elastic modulus	V_m	volume fraction of matrix
E_f	fibre elastic modulus	x	distance of a point from the crack centre
E_m	matrix elastic modulus	x_d	stress transfer distance
f	snubbing coefficient	x_{dn}	stress transfer distance for the n^{th} section
f'	apparent fibre strength reduction coefficient	z	distance of centroid of a fibre from the crack plane
G_d	interfacial chemical bond strength	β	slip-hardening coefficient
$\bar{K}$	ratio of crack tip energy absorption to fibre energy absorption	γ	interfacial frictional bond strength reduction factor
K_B	stress-intensity factor due to fibre bridging	δ	crack opening displacement
K_L	stress-intensity factor due to applied remote load	δ_0	crack opening corresponding to complete debonding
K_m	matrix fracture toughness	δ_{0L}	crack opening corresponding to complete debonding for long embedment side
K_{tip}	crack tip fracture toughness	δ_{0s}	crack opening corresponding to complete debonding for short embedment side
k	parameter used to distinguish cases with different embedment lengths greater or smaller than x_d	ε_{tu}	ultimate tensile train capacity

ΔL	distance between every two adjacent sections	η	ratio of effective fibre stiffness to effective matrix stiffness
L_e	embedment length of fibre	θ	fibre inclination angle
L_L	long embedment side of fibre	θ_{min}, θ_{max}	theoretical minimum and maximum inclined angles of fibres in $p(\theta)$
L_s	short embedment side of fibre	ν	Poisson's ratio of matrix
l_f	fibre length	ξ_n	new factor for calculating τ_{effn} using Eq. (20)
Nc	number of cracks after direct tensile test	σ_b	fibre bridging stress
n	number of meshed sections	$\sigma_b(\delta)$	fibre bridging stress at crack opening displacement δ
n_i	coordinate of each section	σ_c	composite crack strength
$P(\theta)$	bridging force in a single fibre at inclination angle θ	σ_{cn}	local composite crack strength for the n^{th} section
$P(0)$	apparent bridging force perpendicular to the crack surface	σ_{fu}	fibre tensile strength
p_n	2D porosity for the n^{th} section	$\sigma_{fu}(\theta)$	in-situ fibre strength in a single fibre at inclination angle θ
$p(z)$	probability density function of z	$\sigma_{fu}(0)$	in-situ fibre strength without inclination
$p(\theta)$	probability density function of fibre inclining angle	σ_{mu}	tensile stress of matrix
$P_d(\delta)$	pull-out force during the debonding stage	σ_m	m^{th} load step
$P_p(\delta)$	pull-out force during the sliding stage	σ_{tu}	ultimate tensile strength
$P_{friction}$	transferred friction along the fibre-matrix interface	τ	interfacial frictional bond strength
P_{pulley}	transferred pulley force at the exit point	τ_{effn}	effective interfacial frictional bond strength for the n^{th} section
P_{peak}	peak pull-out force at complete debonding of aligned fibre under single fibre pull-out test	τ_0	initial frictional bond strength
r_a	equivalent long radius of elliptical shaped pore	$\tau(\delta)$	interfacial frictional bond strength increase due to the slip-hardening behaviour
r_b	equivalent radius of circular shaped pore		

1. Introduction

As a novel class of high-performance fibre reinforced cementitious composites, engineered cementitious composites (ECC), also called strain-hardening cementitious composites (SHCC), is a promising construction material with high tensile ductility and crack resistance leading to the name of "bendable concrete" for the layman [1]. ECC exhibits prominent strain-hardening behaviour along with multiple cracking characteristics, which is designed (or "engineered") based on micromechanics to overcome the inherent brittleness of ordinary cement-based materials [2, 3]. The ultimate tensile strain capacity and compressive strength of ECC reinforced with different short-cut fibres such as polyvinyl alcohol (PVA), polyethylene (PE), polypropylene (PP) fibres and hybrid fibres at 2% (by volume) are reported to be 3-8% and 20 -160 MPa, respectively [4, 5]. Among them, PVA and PE fibres are the most widely used. Compared to PVA fibre-reinforced ECC, PE fibre-reinforced ECC (PE-ECC) yields more robust tensile ductility with tensile strain capacity of over 4% and can also maintain a considerable low crack width below 100 μm [6, 7], and thus is more favoured.

ECC is a composite material carefully designed by tailoring the properties of fibres, matrix and fibre-matrix interface. In recent years, a variety of ECCs with different performances such as high-strength high-ductility ECC [8-10], 3D printed ECC [11-15], seawater sea-sand ECC [10, 16, 17], engineered geopolymer composite [18-21], self-healing ECC [22-24], and self-stressing ECC [25-28] have been successfully developed based on micromechanical modelling together with associated experimental work. In recent years, a number of numerical methods (lattice-type fracture model, finite element model (FEM), etc) and micromechanics-based analytical models have been used to analyse the multiple-cracking and strain-hardening behaviour of ECC. For the numerical method, lattice-based models were used to simulate the crack development and strain-hardening behaviour of ECC in tension, where the material was discretised as a network of truss or beam elements with linear elastic properties before first cracking and followed by a linear piecewise post-cracking curve with softening branches [29-31]. Huang et al. [32] developed a two-dimensional extended finite element model (XFEM) combined with a cohesive zone model to simulate the tensile behaviour of ECC using a simplified tensile constitutive law consisting of yielding, hardening and softening phases, where each cohesive zone was adaptively embedded into the XFEM prospective element upon the cracking. To simplify the calculation process, a one-dimensional XFEM based approach was further proposed by neglecting the width and thickness of ECC to predict the tensile behaviour of ECC [33]. In this method, only one crack was assumed to form at the centre of each meshed element when its tensile stress exceeds the local crack strength. To capture the crack patterns during tensile loading, an efficient discrete model for ECC was proposed by Shi and Leung [34] to simulate the direct tensile test using continuum element for matrix damage/cracking, truss element for fibre bridging effect and interface element for matrix-fibre interaction. Since the above models are mainly used for structural

behaviour simulation, they will not be the focus of the present study.

Since the early 1990s, different micromechanics-based analytical models were developed by considering the multiple cracking criteria, the force transfer mechanism between fibre and matrix as well as fibre bridging stress versus crack-opening relationship for a single crack, and the composite tensile behaviour [35-41]. For instance, Lu and Leung [42] proposed a micromechanics-based model to simulate the multiple cracking behaviour of ECC accounting for the effects of non-uniform matrix strength, post-cracking increase in fibre bridging stress and fibre rupture on stress transfer. Subsequently, the chemical bond, slip-hardening behaviour and fibre rupture were also considered in the analysis of the stress field in the matrix [43]. In Ref. [44], a micromechanics-based stochastic model was developed to capture the variability of tensile behaviour of ECC induced by the heterogeneity of material microstructure composed of fibre, matrix, and fibre-matrix interface. Thereafter, through considering the chemical bond and slip-hardening behaviour of fibre-matrix interface and two-way fibre pull-out, a generic model was further adopted to determine the crack spacing of ECC with randomly oriented polymeric fibres [45]. It was demonstrated that stress transfer distance related to the determination of crack spacing is an important property governing the tensile strain capacity of ECC, and the actual random distribution characteristics of key factors should be considered to improve the accuracy of predictions [46-51].

As a heterogeneous material, the multiple cracking behaviour of ECC is highly dependent on different micromechanical constituent parameters, mainly including fibre, matrix, and fibre-matrix interfacial properties. Among them, the interfacial frictional bond strength is a critical parameter as it would affect the crack strength of ECC as well as the fibre bridging stress and cracking spacing. It was found that the interfacial frictional bond strength reduces with the increase of fibre content [40]. Hence, a reduction coefficient of interfacial frictional bond strength can be introduced to account for this phenomenon and determine an effective interfacial frictional bond strength for each cross-section of ECC specimens. In Ref. [52], the ratio of the exposed surface area of an elliptical fibre strand along its circumference to the area of total fibre surface area per strand was defined as the reduction factor, whereas it accounts for the bundling effect (a non-uniform distribution of fibres) but not the fibre dosage variation. As the heterogenous microstructure of ECC in terms of pore structure as well as fibre dosage, orientation and distribution lead to the variation of tensile behaviour of ECC. Ignoring the spatial distribution of pores in the matrix, and the non-homogeneity of fibre volume fraction in ECC would result in inaccurate predictions [32, 44]. To date, there is still very limited work in literature on the microstructure-related variation of interfacial frictional bond strength, which needs to be further studied to gain a comprehensive understanding of the unique tensile strain-hardening and multiple-cracking behaviour of ECC. In particular the relationships between pore structure/fibre content and interfacial frictional bond strength has not yet been extensively explored. In the existing

studies, the ideal pore size distribution was adopted to predict the multiple cracking behaviour of ECC, instead of those characterised using non-destructive testing method.

The main purpose of this study is to propose a generic and practical micromechanical analytical model for predicting the strain-hardening behaviour of PE-ECC accounting for the pore structure characteristics and its effect on crack-bridging properties. Firstly, a new model considering the heterogeneity of material property such as variation of local pore size, fibre volume fraction, fibre diameter, fibre location and orientation as well as interfacial frictional bond strength was introduced to determine the crack strength and fibre bridging strength of ECC. The microstructural features of ECC were characterised using advanced techniques including X-ray computed tomography (XCT) and backscattered electron (BSE). Then, different test methods for measuring the essential key micromechanical parameters were briefly presented. Afterwards, single crack direct tensile and uniaxial tensile tests were performed on PE-ECC specimens to validate the proposed model. A series of parametric studies were subsequently carried out to investigate the effects of different design parameters including the interfacial frictional bond strength reduction factor, fibre length, and fibre orientation distribution on the constitutive relationship and crack width distribution of PE-ECC, based on which the underlying mechanisms were explored and discussed in depth.

2. Probabilistic multiple cracking model

In order to accurately simulate the ECC multiple cracking process, the composite crack strength and fibre bridging strength should be determined from micromechanics, and the heterogeneity of material parameters should also be properly considered. Herein, a simplified analytical model for predicting the crack strength of ECC is firstly proposed by assuming that the pores in the matrix are not bridged by fibres initially. Then, the fibre bridging strength based on the constituents' properties and stress transfer distance are employed to determine the sequential formation of multiple cracking. Finally, the overall modelling procedure of the proposed model is further summarized in detail.

2.1 Crack strength

Crack strength of ECC is defined as the tensile stress at the formation of a through crack, which is influenced by both the fracture toughness of matrix and fibre bridging, while the crack initiation and growth are caused by internal pores and the interface between sand and cement paste in ECC [53-55]. Existing models for predicting the crack strength of ECC including randomly arranged short fibres are shown in **Fig. 1a**. A parabolic crack with the crack (pore) size of c was assumed to have uniform crack-bridging stress on the crack flanks for a penny-shaped crack bridged by fibres, and the crack tip fracture toughness (K_{tip}) is the sum of the components related to the applied tensile load (K_L) and the fibre bridging (K_B) [36] which can be determined by:

$$K_{tip} = K_L + K_B = \frac{E_c}{E_m} K_m \tag{1}$$

$$K_{tip} = 2\sqrt{\frac{c}{\pi}}\int_0^1 \frac{[\sigma_L - \sigma_b(\delta(X))]XdX}{\sqrt{1-X^2}} = 2\sqrt{\frac{c}{\pi}}\int_0^1 \frac{\sigma_L XdX}{\sqrt{1-X^2}} - 2\sqrt{\frac{c}{\pi}}\int_0^1 \frac{\sigma_b(\delta(X))XdX}{\sqrt{1-X^2}} \quad (2)$$

where E_c is the composite elastic modulus, E_m is the matrix elastic modulus, σ_b is the fibre bridging stress, $X = x/c$ with x denoting the distance of a point from the crack centre, K_{tip} can be simply regarded as the matrix fracture toughness (K_m) for the composite with low fibre dosage, and $\delta(x)$ is the crack opening that can be expressed as [56]:

$$\delta(x) = \sqrt{\frac{c}{\pi}}\frac{4(1-\nu^2)K_{tip}}{E_c}\sqrt{1-\left(\frac{x}{c}\right)^2} \quad (3)$$

where ν is the Poisson's ratio of matrix, and $E_c = E_m V_m + E_f V_f$ with V_m, E_f and V_f representing the volume fraction of matrix, the elastic modulus of fibre and the volume fraction of fibre, respectively.

By combining Eqs. (1)-(3) and setting $K_{tip} = K_m$, the crack strength (σ_c) of a given cross-section can be obtained as:

$$\sigma_c = g\sigma_0\left[\frac{\sqrt{\pi}}{2}\frac{\bar{K}}{\bar{C}} + \left(\frac{4}{3}\sqrt{\bar{C}} - \frac{1}{2}\bar{C}\right)\right] \quad (4)$$

with

$$g = 2\left(1 + e^{\pi f/2}\right)/(4 + f^2) \quad (5)$$

$$\sigma_0 = V_f\tau\left(l_f/d_f\right)/2 \quad (6)$$

$$\bar{K} = \left(K_{tip}/\sigma_0\sqrt{c_0}\right)/\left(g\tilde{\delta}^*\right) \quad (7)$$

$$\bar{C} = \tilde{\delta}^{*-1}\sqrt{c/c_0} \quad (8)$$

$$c_0 = \left(\frac{l_f E_m}{2K_m}\right)^2 \frac{\pi}{16(1-\nu^2)^2} \quad (9)$$

$$\tilde{\delta}^* = \left(2\tau/E_f(1+\eta)\right)\left(l_f/d_f\right) \quad (10)$$

$$\eta = \left(V_f E_f\right)/(V_m E_m) \quad (11)$$

where $\bar{K}$ is the ratio of crack tip energy absorption to fibre energy absorption, $\bar{C}$ is the normalised crack radius at the peak crack-bridging displacement, f is the snubbing coefficient, τ is the interfacial frictional bond strength, and l_f and d_f are the length and diameter of fibre, respectively.

Once the included micromechanical parameters are given, the crack strength of ECC as a function of pore (crack) size can be determined using Eq. (4). However, as shown in the scanning electron microscope (SEM) images presented in a previous study [57] (see **Fig. 2a**), most pores in PE-ECC were not bridged by fibres, which was also reported in Ref. [58]. Microcracks (see **Fig. 2b** and **Fig. 2c)** can initiate from pores in the matrix or sand/matrix interface and propagate towards the fibres as the applied tensile load increased while the fibres would begin to restrict the crack growth. For pores (or sand/matrix interface) that are not bridged by fibres, the analytical model for predicting the crack strength can be modified, as illustrated in **Fig. 1b**, which is also composed of two parts with a minor change in K_L. For the integral variable x, the range of integration for calculating K_B remains

[0, c], while for calculating K_L it is in the range of [0, $c + c_p$], where c_p is the nominal initial pore size without fibre across it and c is the crack size bridged by fibres during crack growth. The stress balance on the crack surface was considered to be associated with the crack shape during crack growth in the original models. As the cracks in the modified model are newly created and the initial defects have no effect on the initial crack opening displacement, such assumption is applicable to the modified model, which can be explicitly calculated as a function of c and c_p as follows:

$$\sigma_c(c, c_p) = g\sigma_0 \left[\frac{\sqrt{\pi}}{2} \frac{\bar{K}}{\tilde{\delta}_*^{-1} \sqrt{(c+c_p)/c_0}} + \left(\frac{4}{3}\sqrt{\bar{C}} - \frac{1}{2}\bar{C} \right) \right] \tag{12}$$

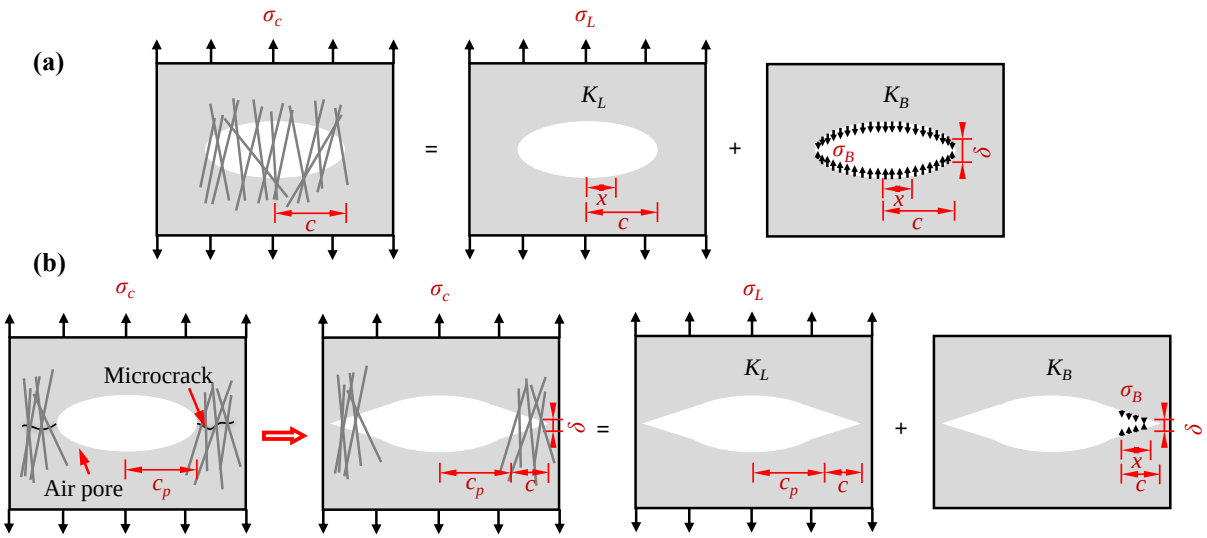

Fig. 1. Schematic illustration of the existing and modified models for determining the crack strength of ECC: (a) existing model and (b) modified model [57].

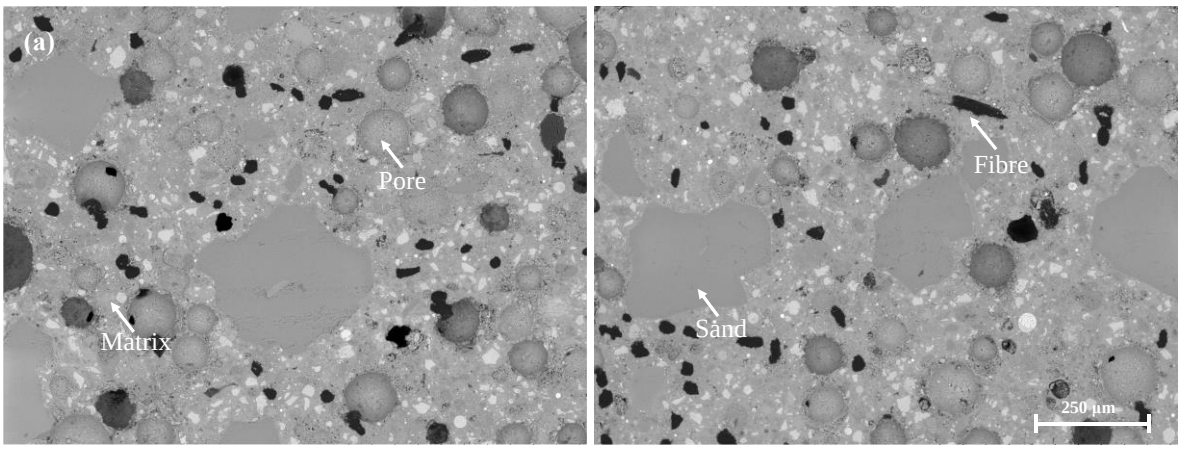

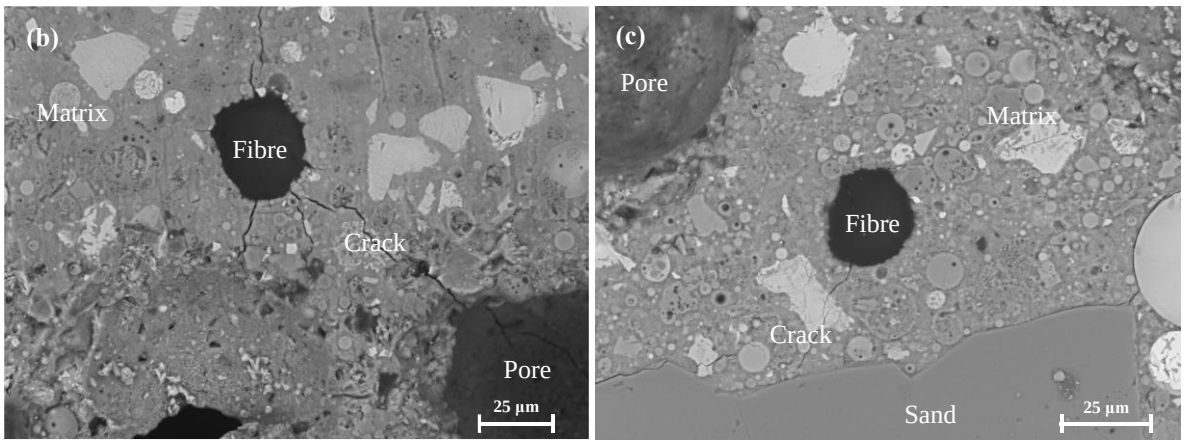

Fig. 2. (a) BSE images of normal ECC with various orientation distribution, (b) microcracks between the fibre, pore and the matrix, and (c) microcracks between the fibre, sand particle and the matrix. [57]

Fig. 3 shows a schematic diagram of the random distribution of pore size, nominal pore size and fibre volume fraction in ECC. Considering an ECC sample under uniaxial tension (**Fig. 3a**), the middle part of the sample is meshed by n evenly spaced sections into (n +1) pieces. In this study, the 80 mm long gauge region is divided into 399 sections, and thus the distance between every two adjacent sections ΔL is set to be 0.2 mm, which is consistent with that given in Ref. [43]. The coordinate of each section can be denoted as n_i (i = 1, 2, … n). More than one pore is randomly distributed in each cross-section, which is nearly elliptical in shape. To calculate the cracking strength for each pre-defined section based on the microstructural information obtained, the following assumptions are made:

(I) Only the pore with the largest area in each cross-section can cause cracking, i.e., the crack strength is dominated by the largest pore while the presence of smaller pores has less influence, according to a previous work [43]. The pores are not bridged by fibres. Even if a fibre passes through the pores (**Fig. 3b**), the actual embedment length becomes shorter (similar to the effect of matrix spalling of an inclined fibre with the inclination of θ [59]) and the fibre will be pulled out prematurely. For two sections (sections 1 and 2 in **Fig. 3b**) with the same area of the largest pore, it is possible to obtain different results if assuming the crack size in elliptical shape with semi-axis r_a and circular shape with radius r_b. Hence, the equivalent long radius of the ellipse and the equivalent radius of the circle detected by X-ray computed tomography (XCT) scanning are regarded as the crack size for the calculation of crack strength using Eq. (12).

(II) The fibres are uniformly dispersed in each section and the bundling effect can be ignored [52].

(III) The difference in porosity of the cross-sections is used to set the local fibre volume fractions. The section with median porosity corresponds to a fibre volume fraction of 2% and the typical linear relationship between porosity and fibre volume fraction was used in this study. For sections 1, 2, and

3 in **Fig. 3b**, sections 1 and 2 have the same porosity (i.e., the total area of all pores is equal), while the section 1 has a greater porosity than section 3. Thus, it can be estimated that the local fibre volume fractions of sections 1 and 2 are the same and smaller than that of section 3, i.e., $V_{f1} = V_{f2} < V_{f3}$. Note that this assumption for calculating the bridging stress versus crack opening relation is valid after the first crack is formed.

(IV) The reduction factor of interfacial frictional bond strength is linearly related to fibre volume fraction and the apparent frictional bond strength decreases with the increase of fibre volume fraction [40, 60]. For the n^{th} section, a new factor (ξ_n) was introduced to describe the relationship between the effective interfacial frictional bond strength (τ_{effn}) and the initial frictional bond strength (τ_0), which can be expressed as:

$$\tau_{effn} = \tau_0 \cdot \xi_n \tag{13}$$

$$\xi_n = -\gamma \cdot V_{fn} + 1 \tag{14}$$

where V_{fn} is the local fibre volume fraction for the n^{th} section (no higher than 2% for typical ECC), and γ is the interfacial frictional bond strength reduction factor that is set as 21 for the control specimen based on the experimental data. More details about the effect of this factor on the prediction results of the direct tensile test are given in **Section 5**.

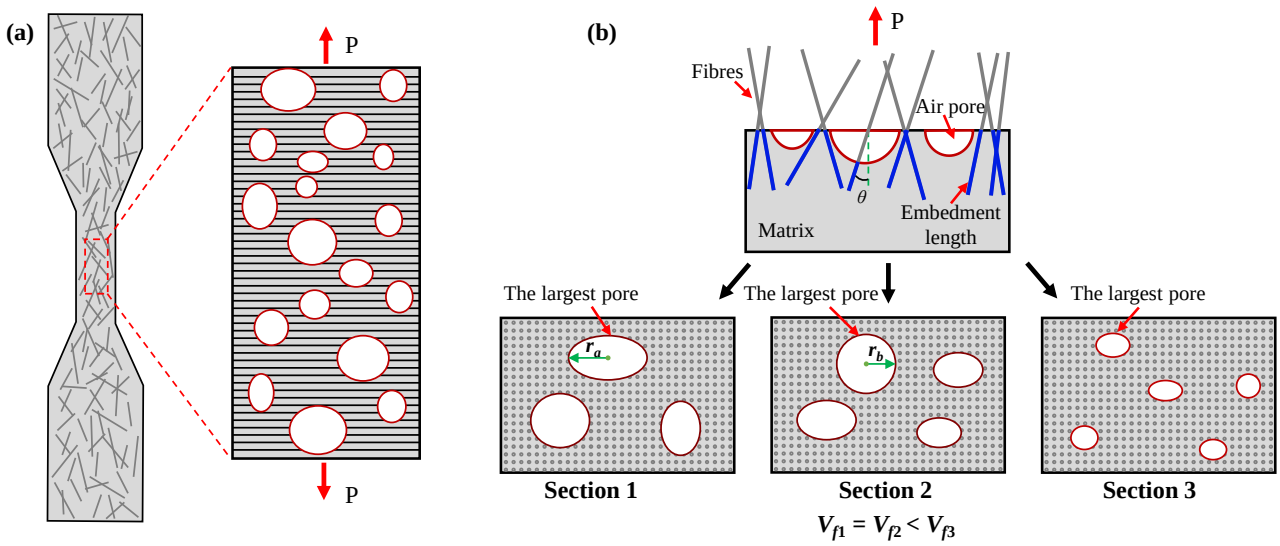

Fig. 3. Schematic diagram of (a) the randomly distributed pore size, and (b) the nominal pore size and fibre volume fraction in ECC.

Based on the above simplifying assumptions, it is possible to establish a unified quantitative relationship between pore structure characteristics (pore size and porosity) and cross-section micromechanical parameters such as local fibre volume fraction (V_{fn}), effective interfacial frictional bond strength (τ_{effn}), and crack strength (σ_{cn}) for the n^{th} section. In this study, the variability of V_{fn} and τ_{effn} is considered when calculating the crack strength and the other parameters included in Eq. (12) are taken as the mean values following a uniform distribution.

Fig. 4 shows the initial nominal pore size distribution and 2D porosity for each section (p_n) of

PE-ECC samples obtained from XCT and presented in a previous study [57]. The distribution of porosity and equivalent pore size conforms to the Weibull distribution. The 2D porosity and nominal pore size for equivalent circular radius and equivalent elliptical long radius in PE-ECC are mainly in the ranges of 0.5-4.5%, 0.25-1.75 mm and 0.25-2.25 mm, respectively. The nominal pore size is continuously distributed on the set of 399 sections along the ECC sample. Then, the local fibre volume fraction on each section of ECC can be obtained according to the linear correlation between porosity and fibre volume fraction, as shown in **Fig. 5a**, which indicates that the local fibre volume fraction varies continuously between adjacent sections and ranges from 1.88% to 2.03%, with an average fibre volume fraction of 2%. Afterwards, the crack strength for each section can be calculated using Eqs. (12)-(14) by inputting the related parameters, the results of which are presented in **Fig. 5b**. All the parameters used are summarised below. Similar to the distribution of local fibre content, the calculated crack strength for each section also varies continuously and the crack strength calculated using the long half-axis of the equivalent ellipse as the pore size is lower than the equivalent circle radius while the difference is not significant. The first crack strengths for the equivalent circle radius and the equivalent elliptical long radius are found to be 2.68 MPa and 2.35 MPa, respectively.

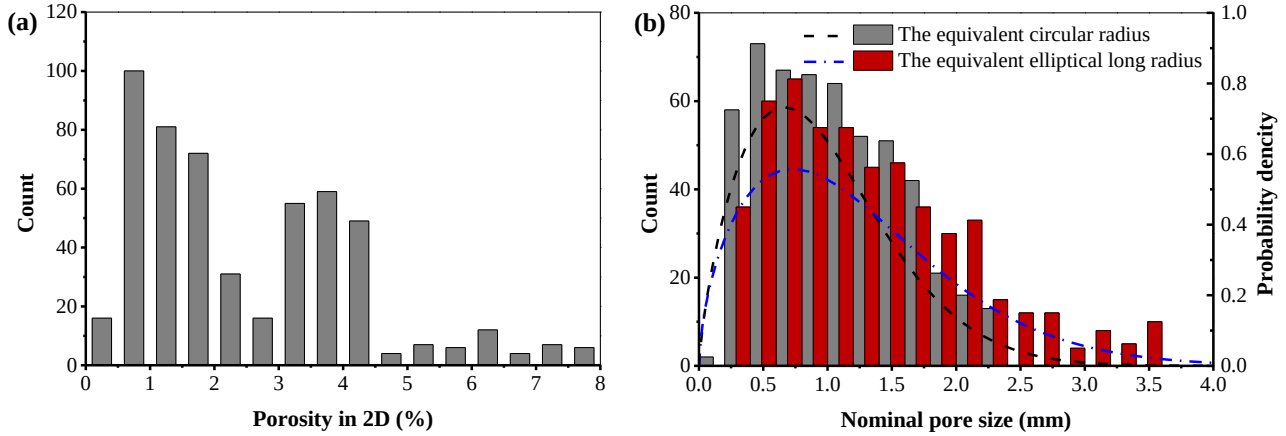

Fig. 4. (a) Initial 2D porosity distribution, and (b) initial nominal pore size distribution in PE-ECC.

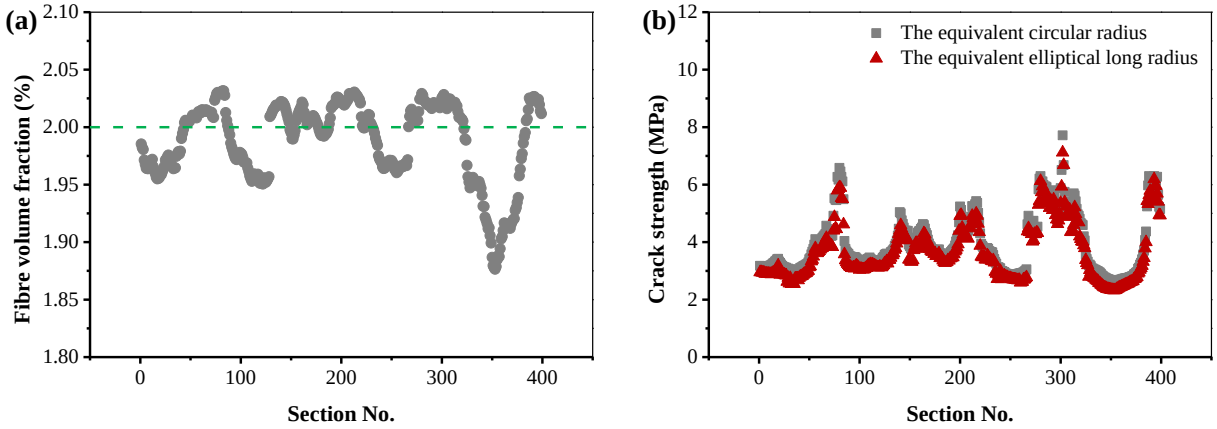

Fig. 5. (a) Nominal local fibre volume fraction, and (b) calculated crack strength for each section of PE-ECC.

2.2 Crack bridging stress and strength

The relationship between the average stress of the fibres bridging two sides of the crack (σ_b) and the crack opening displacement (δ) can be assessed by calculating and summing up the stress-crack opening relations of all bridging fibres with various dispersion and orientation. The fundamental stress-crack opening relationships adopted in this study are collected from Refs. [40] and [61] while the focus is placed on the mechanisms of fibre rupture and two-way fibre debonding and one-way pull-out for PE-ECC. For the design of ECC, the fibre bridging relationship is crucial as it is highly associated with the microstructure of ECC and directly governs the macroscopic tensile strain-hardening behaviour. The determination of the fibre bridging relationship for PE-ECC is explained in detail below.

2.2.1 Single fibre pull-out

The σ_b-δ laws are determined based on the process of fibre pull-out from the matrix after cracking as the fibres would undergo a debonding stage when subjected to pull-out force. As illustrated in **Fig. 6**, the fibre segment that bridges the crack is assumed to be perpendicular to the crack surface. Assuming constant initial frictional bond strength (τ_0) and interface chemical bond strength (G_d), the pull-out force during the debonding stage, $P_d(\delta)$, can be described as:

$$P_d(\delta) = 2\pi\sqrt{\frac{\tau_0 E_f d_f^3(1+\eta)}{2}\delta + \frac{G_d E_f d_f^3}{2}}, 0 \le \delta \le \delta_0 \tag{15}$$

$$\delta_0 = \frac{2\tau_0 L_e^2(1+\eta)}{E_f d_f} + \sqrt{\frac{8G_d L_e^2(1+\eta)}{E_f d_f}} \tag{16}$$

where $\eta = V_f E_f / V_m E_m$ is the ratio of effective fibre stiffness (accounting for volume fraction) to effective matrix stiffness, E_f is the fibre elastic modulus, δ_0 is the crack opening corresponding to complete debonding, and L_e is the embedment length of the given fibre (note that only the fibres with positive embedded length would provide the crack-bridging action).

After debonding, the fibres enter the sliding stage, and the interface is completely controlled by friction. The frictional stress is assumed to be linearly related to the slip distance and the slip-hardening coefficient (β) is used to describe the hardening phenomenon during sliding. The pull-out force during the sliding stage, $P_p(\delta)$, can be expressed as:

$$P_p(\delta) = \pi\tau_0(L_e - \delta + \delta_0)\left(d_f + \beta(\delta - \delta_0)\right), \delta_0 \le \delta \le L_e \tag{17}$$

Due to the random dispersion of numerous fibres in ECC, the fibres on the crack surface would lead to additional friction with the matrix. For flexible fibres, the Eulerian rein theory can be used to estimate the effect of fibre inclination on the increase of apparent bridging force ($P(\theta)$) as follows [62]:

$$P(\theta) = P(0)e^{f\theta} \tag{18}$$

where θ is the fibre inclination angle concerning tensile loading direction, $P(0)$ is the apparent

bridging force perpendicular to the crack surface, and f is the empirical snubbing coefficient determined from experiments.

In addition, Kanda and Li [63] proposed a strength reduction coefficient (f') to account for the reduction of in-situ strength of fibres, as follows [46]:

$$\sigma_{fu}(\theta) = \sigma_{fu}(0)e^{-f'\theta} \tag{19}$$

where $\sigma_{fu}(0)$ is the in-situ fibre strength without inclination.

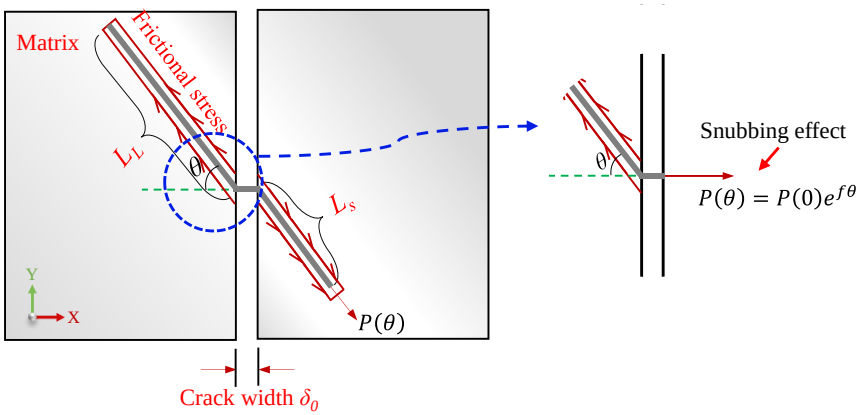

Fig. 6. Schematic illustration of the short embedment fibre under full debonding.

2.2.2 Two-way debonding and one-way pull-out

G_d can be considered to be approximately zero for PE-ECC due to the hydrophobic nature of the PE fibre, and thus Eq. (16) can be re-written as:

$$\delta_0 = \frac{2\tau_0 L_e^2(1+\eta)}{E_f d_f} \tag{20}$$

where $L_e = L_L$ for the long embedment side of the fibre, and $L_e = L_s$ for the short embedment side, as illustrated in **Fig. 6**. δ_{0L} and δ_{0s} can be defined as the crack opening corresponding to complete debonding for long and short embedment sides, respectively.

Before complete debonding, $\delta = \delta_L + \delta_s$ and $\delta_L = \delta_s$. After that, the short sides of PE fibres undergo the slipping stage. Owing to the significant slip-hardening behaviour of PVA fibre, fibres may be ruptured during the debonding under the pull-out load of P_{dc} (point B) or slipping stage under the pull-out load of P_{ds} (point C), as shown in **Fig. 7**. However, for PE-ECC, fibre rupture can only occur at the debonding stage under P_{dc} (point A), i.e., one-way fibre pull-out, due to a very small slip-hardening response with β close to zero as observed from experiments (see **Section 3.3**). The pull-out load of PE fibres is controlled by interfacial friction throughout the whole pull-out process. During the debonding stage, PE fibre rupture would occur if the fibre bridging stress ($\sigma_b(\delta)$) exceeds the in-situ fibre strength ($\sigma_{fu}(\theta)$) at a given inclination angle, otherwise, the short side of the fibre would be completely pulled out from the matrix.

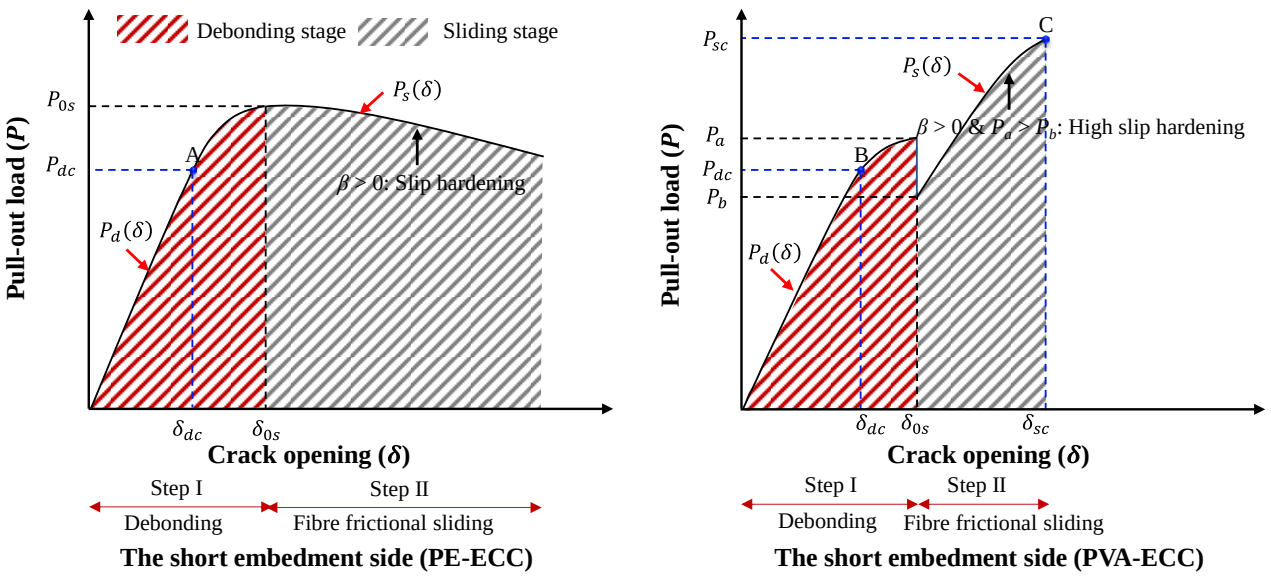

Fig. 7. Illustration of the fibre situation when the fibre rupture occurs during pull-out: load (P) against crack opening (δ) of the short embedment side.

2.2.3 Average bridging stress

After determining the debonding and slipping forces of single fibres, the composite bridging stress $\sigma_b(\delta)$ against crack opening (δ) for a single crack can be derived by integrating the contribution of individual fibres as follows:

$$\sigma_b(\delta) = V_f \int_0^{\pi/2} \int_0^{(l_f/2)\cos\theta} \sigma(\delta,\theta,z)p(z)p(\theta)dzd\theta \quad (21)$$

where V_f is the fibre volume fraction, l_f is the fibre length, z is the distance of centroid of fibre from the crack plane (as illustrated in **Fig. 8**), $p(z)$ is the probability density function of z, and $p(\theta)$ is the probability density functions of the fibre inclining angle, which can be expressed as [46, 64]:

$$p(z) = \frac{1}{l_f}, -\frac{l_f}{2} \le z \le \frac{l_f}{2} \quad (22)$$

$$p(\theta) = \frac{\{\sin\theta\}^{2r-1}\{\cos\theta\}^{2q-1}}{\int_{\theta_{min}}^{\theta_{max}} \{\sin\theta\}^{2r-1}\{\cos\theta\}^{2q-1}d\theta} \quad (23)$$

where r and q are the shape parameters, θ_{min} and θ_{max} are the theoretical minimum and maximum inclined angles of fibres (θ_{min} = 0 and θ_{max} = π/2). In particular, $r = q = 0.5$ stands for 2D random distribution (i.e., $p(\theta) = 2/\pi$), $r = 1$ and $q = 0.5$ denotes 3D random fibre distribution (i.e., $p(\theta) = sin\theta$), and $r \geqslant 0.5$ and $q > 0.5$ represents other general cases.

2.3 Stress transfer distance

Stress transfer distance or crack spacing (x_d) is defined as the distance necessary to fully transfer stress from bridging fibres in a cracked surface back to the matrix through the fibre-matrix interface. The stress in the matrix within x_d is lower than the matrix tensile strength and no crack would form in this region. A micromechanics-based model for x_d presented in Ref. [45] was used in this study to determine x_d, which can well reflect the random distribution of fibre orientation, the snubbing effect

and the fibre debonding and rupture mechanisms for PE-ECC.

As illustrated in **Fig. 9a**, x_d along the crack opening can be derived based on the force equilibrium considering the transferred pulley force (P_{pulley}) at the exit point and the transferred friction ($P_{friction}$) along the fibre-matrix interface (x axis) and the matrix stress, which can be calculated by:

$$\int \pi d_f \tau(\delta) k p(z) p(\theta) dz d\theta + \int P(\delta)\left(e^{f\theta} - \cos\theta\right) p(z) p(\theta) dz d\theta = \sigma_{mu} V_m \times 1 \times 1 \qquad (24)$$

where $k = min\left\{x_d, \frac{l_f}{2}\cos\theta - z\right\}$ is a parameter to distinguish cases with different embedment lengths L_e greater or smaller than x_d (**Fig. 9b**), $\tau(\delta) = \tau_0\left(1 + \beta(\delta - \delta_0)/d_f\right)$ denotes the interfacial frictional bond strength increase due to the slip-hardening behaviour and τ_0 should be substituted by τ_{effn} for the n^{th} cracked plane as defined in Eq. (13), σ_{mu} and V_m stand for the tensile stress and volume fraction of the matrix, and the first and second terms on the left-hand side of Eq. (24) represent the transferred interfacial force and transferred pulley force, respectively.

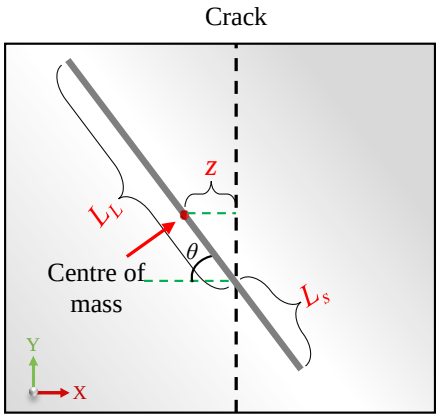

Fig. 8. 2D orientation of crack bridging fibre before debonding.

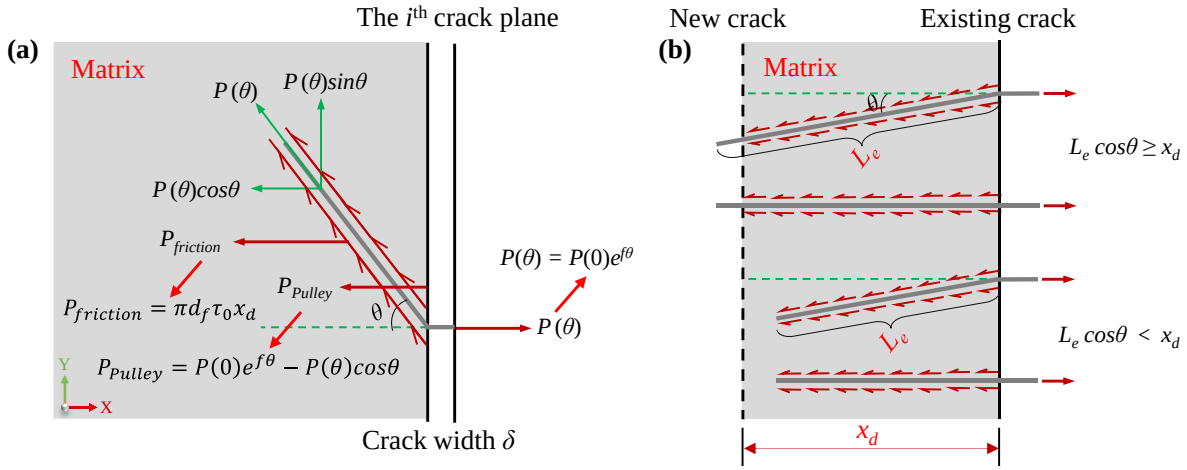

Fig. 9. (a) Force equilibrium at exit point, and (b) fibres with different embedded length.

2.4 Modelling procedure for the multiple cracking process

Fig. 10 shows a flow chart of the use of the proposed micromechanics-based model to simulate the multiple cracking behaviour of ECC. To improve the efficiency of calculations, ECC was loaded at a constant stress increment during strain-hardening stage and the increment of displacement can be approximated by a linear relationship in each incremental interval. Note that a small increment of δ

(0.002 mm) was chosen to compute the single crack bridging strength and Monte Carlo simulation is conducted to generate the fibre bridging stress-crack opening law for each section of ECC considering some key random micromechanical parameters including c_n, z, d_f, θ, τ_{effn}, and V_{fn}.

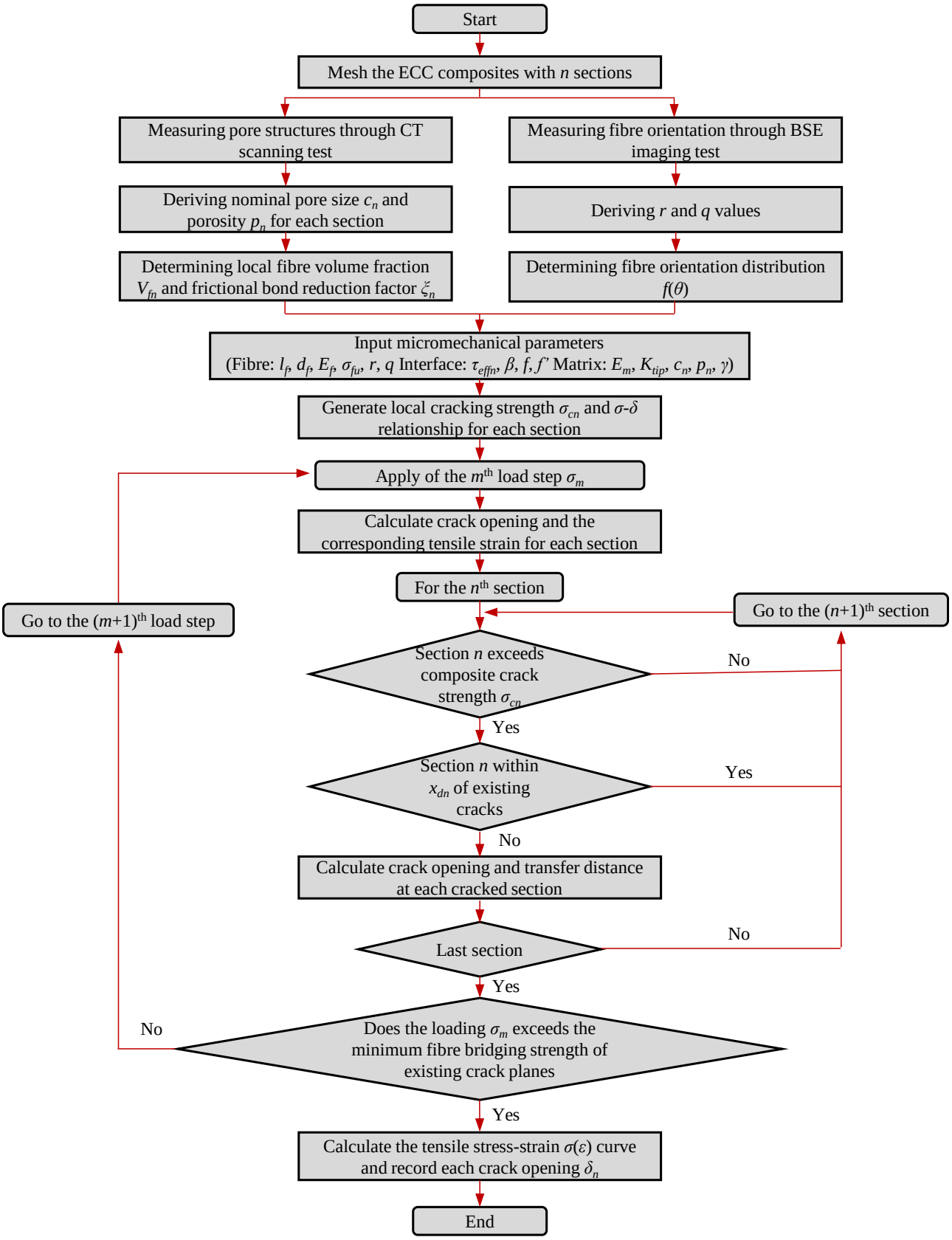

Fig. 10. Flow chart for the prediction of multiple cracking behaviour of ECC using the proposed micromechanics-based model.

3. Determination of micromechanical parameters

To predict the relationship between fibre bridging stress and crack opening (σ-δ curves) of ECC, some input parameters including matrix fracture toughness (K_m), interfacial frictional bond strength (τ_0), slip-hardening coefficient (β) and crack strength (σ_c) as well as pore structure and fibre orientation characteristics need to be determined through a series of tests given below.

3.1 Materials and specimens

The raw materials used in this study to produce ECC include type II 52.5 ordinary Portland cement (OPC), class I fly ash (FA), sulphoaluminate cement (SAC) based on 100% industrial solid wastes, grade 955 silica fume (SF), water, polycarboxylate-based superplasticiser (SP), hydroxypropyl methyl cellulose (HPMC) with a viscosity of 38000-42000 mPa·s, fine quartz sand with a maximum size of 300 μm and a mean size of 100 μm, and chopped PE fibres with lengths of 6 mm and 12 mm. The mix proportion of ECC adopted in this study is presented in **Table 1**.

All fresh mixtures were prepared using a Hobart-type mixer in the laboratory environment (23 ± 1 ℃). First, dry materials including OPC, SF, SAC and fine aggregates were mixed for 2 min at 140 rpm. After that, the water and SP solution were gradually added to the mixer and the fresh materials were mixed at 140 rpm for 3 min. Once a consistent and flowable mixture was reached, the HPMC powder was incorporated, followed by the mixing for 1 min at 140 rpm. PE fibres as needed were then gradually added to the mixer and mixed for 1 min at 140 rpm to achieve uniform fibre distribution. Finally, the fresh mixture was mixed for another 1 min at a high-speed of 420 rpm to complete the mixing procedure and placed in the laboratory environment for 24 h of curing. All specimens were then de-moulded and moved to a room (23 ± 1 ℃ and relative humidity of 40% ± 5%) for curing until the testing age of 28 days.

Table 1 Mix proportion of ECC.

Binder				Sand	Water	SP	HPMC	PE fibre
OPC	SAC	SF	FA					
0.38	0.05	0.09	0.48	0.26	0.26	0.001	0.0004	0.018 (6 and 12 mm)

3.2 Matrix fracture toughness

The matrix toughness of ECC (K_m) can be generally measured using notched beam samples with different sizes as per ASTM E399-12 [65] or RILEM FMC-50 [66]. However, it was found that the calculated crack strength (even ignoring the fibre effect) based on the fracture toughness measured from three-point bending test on a single-edge notched beam is obviously higher than experimental data, which can be explained by the fact that it is difficult to accurately achieve the desired notch size for cementitious materials in practice and the notch produced by the cutter is not an ideal sharp tip but may be a curved surface, leading to inaccurate measurement [67]. As the crack strength (σ_c) of the matix for ECC (without fibre effect) can be calculated using Eq. (25), direct tensile test as per

JC/T 2641-2018 [68] and JSCE [69] was performed on a total of 12 dog-bone shaped plain specimens with a notch at 28 days under a constant loading rate of 0.5 mm/min to obtain and the crack strength from which the matrix fracture toughness can be calculation. The detailed test setup and dimensions of the tested specimen are illustrated in **Fig. 11**. For this specimen, the width of the notch is relatively large and failure can be taken to initiate from flaws in the unnotched section. From experimental observation, the formed crack is limited to a narrow band.

$$\sigma_c = \frac{K_{tip}}{2}\sqrt{\frac{\pi}{c}} \tag{25}$$

where K_{tip} is the crack tip fracture toughness (MPa·m$^{1/2}$) that can be simply regarded as K_m for the composite with low fibre dosage, and c is the nominal pore size (mm) that is the equivalent circle radius of the largest pore on the fracture surface. More details about the relationship between crack strength and nominal pore size for PE-ECC can be found in previous studies [43, 57].

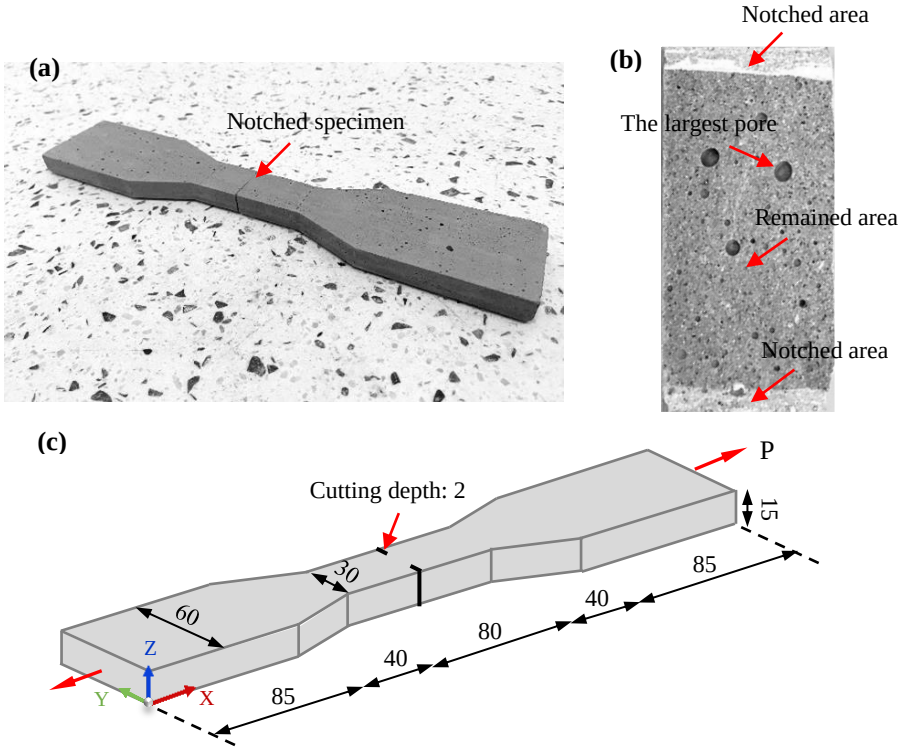

Fig. 11. Direct tensile test for measuring fracture toughness of ECC matrix: (a) notched plain specimen, (b) fracture surface, and (c) dimensions of specimen (in mm).

The maximum pore size at each fracture section and crack strength recorded for each specimen were used to derive the matrix fracture toughness by fitting the measured data with Eq. (25), as shown in **Fig. 12**, indicating a matrix fracture toughness of 0.118 MPa·m$^{1/2}$ and a correlation coefficient of 0.91, which suggests a strong correlation between the crack strength and nominal pore size and thus the obtained fracture toughness can be used for calculating the crack strength of each ECC section. Moreover, the elastic modulus of the ECC matrix (E_m) at 28 days was also measured using prism samples in accordance with ASTM C469 [70], which was found to be 18 GPa.

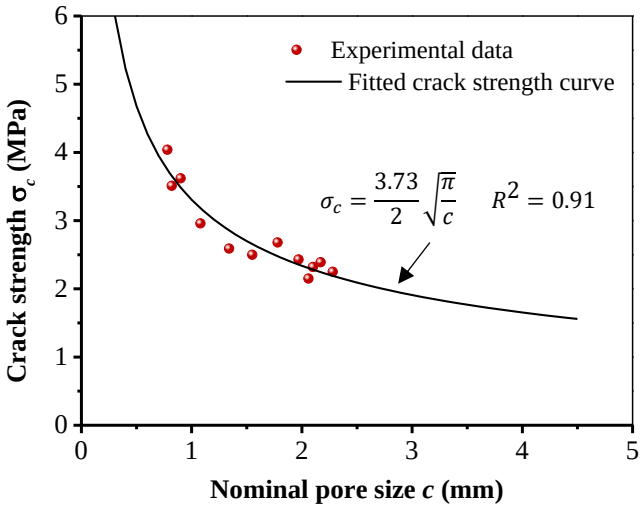

Fig. 12. Crack strength against nominal pore size used to derive the matrix fracture toughness.

3.3 Fibre-matrix interfacial properties

Aligned single fibre pull-out tests were conducted to measure the fibre-matrix interfacial properties including initial interfacial frictional bond strength (τ_0), chemical bond strength (G_d) and slip-hardening coefficient (β), as shown in **Fig. 13**. To improve the testing efficiency, a dedicated mould was designed and used for single fibre pull-out tests. Specifically, the internal dimensions of each opening in the mould is 25 mm × 10 mm × 5mm. When placing the single long fibres, draw a scale line at the centre of the short side of each middle plate for positioning. Then, place the single long fibre along the scale line and perpendicular to the short side of the opening. Afterwards, both ends of the fibre were fixed on the base plate with the tape to keep fibre straight when pouring the ECC matrix into the mould. A thin mould thickness was adopted as it can minimise the number of air pores in the matrix when pouring fresh mortar (i.e., ECC matrix), resulting in a smaller scatter of test curves. Before testing, 2 notches with 3 mm depth were cut by using a precision saw at a set distance of 5 mm from the short side of the specimen, and the entire upper surface of the specimen was fixed by a small steel plate. Owing to the precision of the cutting tool, the actual embedded length of the fibres ranged from 5 mm to 6 mm. In this way, two fibre pull-out curves can be obtained for one specimen. Single fibre pull-out tests were performed using a high-precision electromechanical test system with a maximum load capacity of 4.903 N and force reading accuracy of 1/10000 [71]. The free end of the fibre was glued to a small ball as loading point and the distance from the ball to the flat surface of the specimen was set to approximately 3 mm to avoid the displacement deviation induced by the fibre elongation. After the fully solidifying of quick-drying epoxy glue, the aligned single fibre (inclination angle $\theta = 0°$) was pulled out at a constant loading rate of 0.005 mm/s. A total of 14 typical pull-out load-displacement curves were obtained to determine the fibre-matrix interfacial properties. Due to the hydrophobic nature, the interfacial chemical bond strength was assumed to be zero for PE fibres [41]. The interfacial frictional bond strength (τ_0) and slip-hardening

coefficient (β) can be determined from the single fibre pull-out tests according to [63, 72]:

$$P_{peak} = \pi d_f \tau_0 L_e + \sqrt{\pi^2 G_d E_f {d_f}^3 / 2} \tag{26}$$

$$P_{peak} = \pi d_f \tau_0 [1 + \beta(u - u_0)][L_e - (u - u_0)]e^{f\theta} \tag{27}$$

where P_{peak} is the peak pull-out force at complete debonding of aligned fibre (N), d_f is the fibre diameter (μm), L_e is the fibre embedment length (mm), E_f is the fibre elastic modulus (GPa), u is the pull-out displacement (mm), u_0 is the pull-out displacement at peak force (mm), f is the snubbing coefficient, and θ is the inclination angle of the fibre (radians).

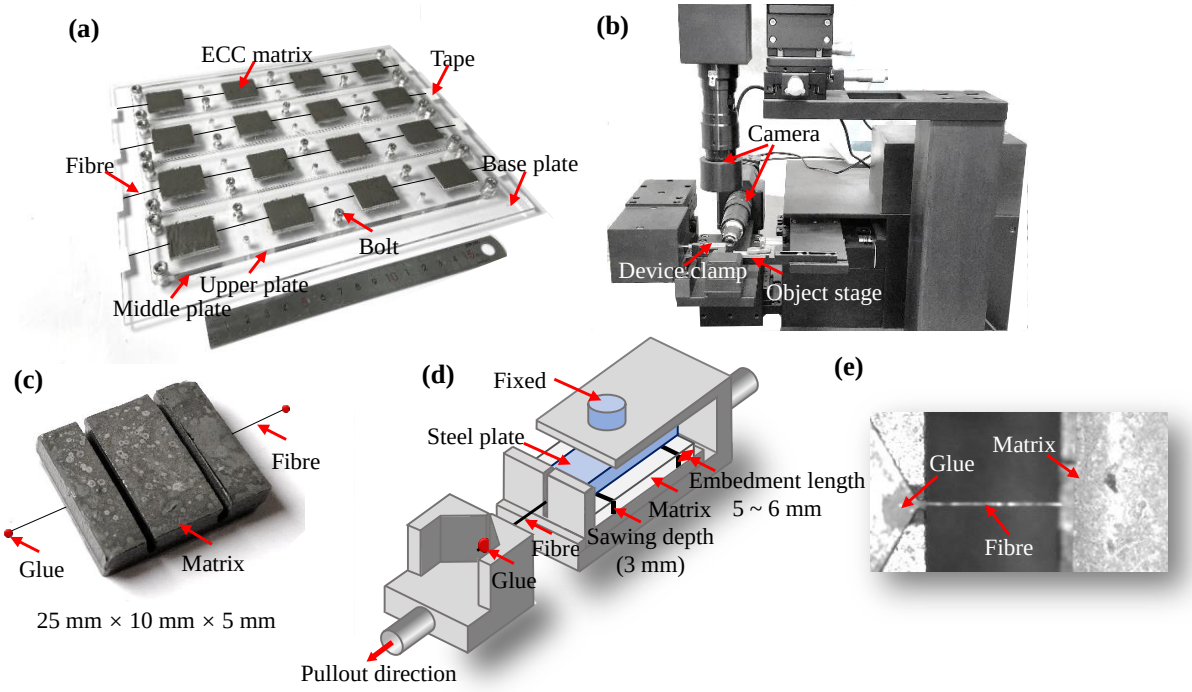

Fig. 13. Sample fabrication and setup of single fibre pull-out test (a) dedicated mould for producing the samples, (b) single fibre pull-out testing system, (c) prepared sample, (d) schematic diagram of the sample to be tested, and (e) snapshot taken during the testing process.

Fig. 14 displays the typical force-slip curves obtained from single PE fibre pull-out tests. The 28-day compressive strength of ECC is 49.17 MPa, which can be classified as normal-strength ECC [73]. All aligned PE fibres were pulled out from the ECC matrix with no significant slip-hardening and thus the fibre fracture is less likely to occur. The bridging stress-crack opening displacement curve decreased slowly after reaching the peak load. **Fig. 15** shows the SEM images of a single fibre pulled out from the ECC matrix, from which more severe fibre abrasion can be observed with the increasing fibre embedded length, which can be ascribed to the fibre delamination effect and the long embedment length of the fibre in the matrix [74]. Based on the force-slip curves plotted in **Fig. 14**, the interfacial frictional bond strength between fibre and matrix can be determined as 1.16 ± 0.3 MPa (see **Table 2**). Moreover, the average slip-hardening parameter for PE fibre in ECC used in this study is 0.004 with a standard deviation of 0.00028, which is approximately two orders of magnitude lower

than that for PVA fibre reinforced ECC [38], which can be attributed to the greater abrasion resistance of PE fibre compared to PVA fibre. In addition, the calculated average slip-hardening coefficient value is close to those reported in Refs. [41, 74]. The mean values of interfacial frictional bond strength and slip-hardening parameter were used as inputs for predictions in the next section.

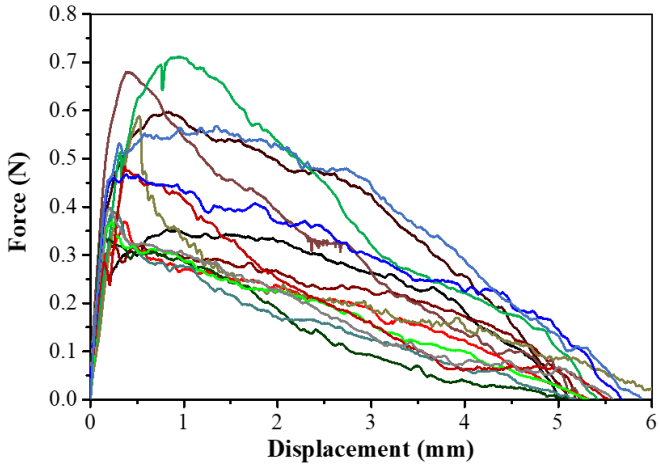

Fig. 14. Force-slip curves obtained from single fibre pull-out tests on PE-ECC.

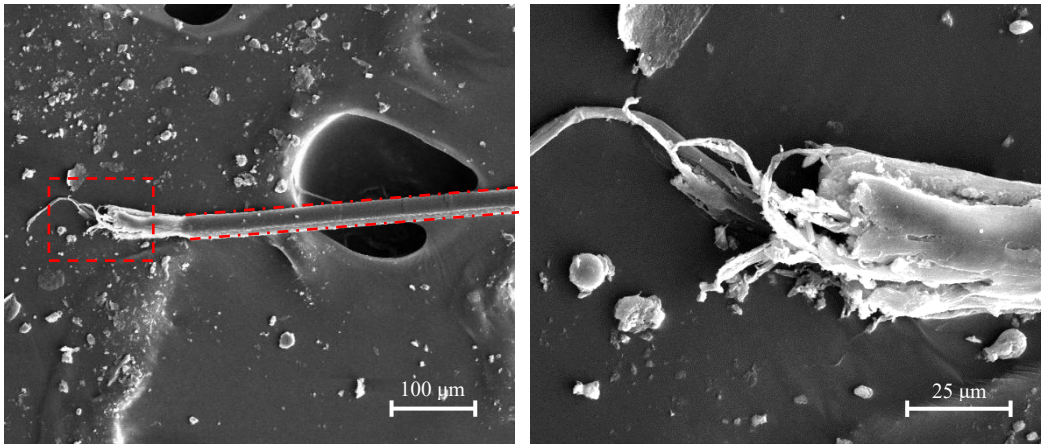

Fig. 15. SEM images of PE fibre pulled out from ECC matrix.

Table 2 Micromechanical parameters of PE-ECC used as inputs for predictions.

Phase	Parameters	Value
Fibre	Length, l_f (mm)	6 and 12[a]
	Diameter, d_f (μm)	23.86 ± 4.44[b]
	Elastic modulus, E_f (GPa)	110[a]
	Tensile strength, σ_{fu} (MPa)	3000[a]
	Interfacial chemical bond, G_d (J/m^2)	0[c]
	Orientation distribution (r, q)	r = 5, q = 3.8[d]
Matrix	Elastic modulus, E_m (GPa)	18[b]
	Fracture toughness, K_{tip} (MPa·m$^{1/2}$)	0.118[b]
	Poisson's ratio, v	0.2[b]
Fibre-matrix interface	Initial interfacial frictional bond strength, τ_0 (MPa)	1.16 ± 0.3[b]
	Slip-hardening coefficient, β	0.004[b]
	Snubbing coefficient, f	0.65[e]

Fibre strength reduction factor, f'	0.50[f]
Frictional bond reduction factor, γ	20[g]

[a] Nominal properties obtained from the fibre supplier. [b] Measured value in this study. [c] Assumed to be zero for PE fibres with hydrophobic surface. [d] Derived from Eq. (23) based on the measured data in Ref. [57]. [e] Li et al [75]. [f] Li et al [76]. [g] Value assumed for this study.

3.4 Microstructural characteristics

XCT technology and BSE imaging along with image processing and analysis were undertaken to investigate the microstructural characteristics of ECC in terms of pore structure and fibre orientation. The detailed information on XCT and BSE imaging can be found in a previous study [57]. Based on the microstructural characteristics obtained, the relevant micromechanical parameters of PE-ECC can be derived according to the procedures given in **Section 2**, which are also summarised in **Table 2**.

4. Validation of predictions with experimental data

4.1 Comparison between predictions and experimental results of single crack direct tensile behaviour

To validate the predictions using the input parameters listed in **Table 2** with experimental results, single-crack tests on notched mould-cast PE-ECC specimens under direct tension were carried out to generate a single crack and obtain the bridging stress-crack opening (σ-δ) curves, the detailed information of the specimen configuration and test setup was given in Ref. [57]. The predicted σ-δ curve for each section and the fibre status in PE-ECC can be calculated by combining Eqs. (15) - (23) related to micromechanical principles in **Section 2** and inputting parameters given in **Table 2**. **Fig. 16a** shows the measured and predicted σ-δ curves for PE-ECC with specific microstructural features described in **Section 3**. The distribution of the predicted peak bridging stress for all sections is close to the actual test results (within the measured peak bridging stress scatter, see the grey area in **Fig. 16a**), which indicates that the key micromechanical parameters adopted in this study are reasonable. Specifically, the peak bridging stress predicted through 10 repeated Monte Carlo simulations varied from 4.351 MPa to 4.900 MPa, while the measured peak bridging stress was in the range of 4.248-6.181 MPa. The dispersion of σ-δ curves became higher than the representative simulation results, which can be ascribed to the constant mean value of initial interfacial frictional bond strength (1.16 MPa) used for simulations. Single crack test results indicated the crack-bridging capacity at each crack plane, which would be highly associated with pore structure, local fibre volume fraction, and other factors that can affect the effective interfacial frictional bond strength. As the value of τ_0 has a significant influence on the tensile strain capacity [44], the upper and lower bounds of the measured σ-δ curves can be well-estimated by taking the τ_0 value obtained from single fibre pull-out tests as random variables, ranging from 0.86 MPa to 1.46 MPa. The effect of interfacial friction bond on the

prediction results will be further discussed in **Sections 4.2** and **5.1**. In addition, it should be noted that the predicted crack-opening displacement at the ultimate bridging stress was much smaller than the measured data. This can be explained by the fact that the range of deformation measured by clip-on gauges attached on two sides of the specimen is actually an area (around the crack plane) not strictly a single crack, but possibly a combination of several cracks (one main crack plus several microcracks), as notched samples normally exhibit multiple cracking behaviour. Similar findings were also reported in Refs. [77, 78].

The fibres bridging the crack would be in a different status as the crack opening gradually increases, as illustrated in **Fig. 7**. **Fig. 16b** shows the calculated percentage of all fibres with different statuses as the crack grows. In the figure, "Pulled out" means the short side of the fibre is completely pulled out from the matrix and the fibre cannot transfer stress anymore; "Debond-Debond" denotes both sides of the fibre are in debonding stage; "Debond-Pullout" means the short side of the fibre is being pulled out while the long side is still in the debonding stage; and "Ruptured" means the stress exceeds the fibre in-situ strength and the fibre cannot transfer stress anymore. Specifically, taking the critical crack opening of 72 μm corresponding to the fibre bridging peak stress of 4.72 MPa as an example, most fibres (98.4%) remain in the Debond-Pullout process while 1.0% of fibres are in the Debond-Debond status, and 0.6% are pulled out with no fibre rupture. During the single-crack test, owing to the superior tensile strength and elastic modulus of PE fibre and the desirable compressive strength of the matrix, only 5 fibres rupture took place, suggesting that almost all the fibres were pulled out from the matrix and fibre rupture can be negligible for this kind of ECC. This can also be evidenced by **Fig. 16c** and is consistent with the downward trend of the crack-bridging curves (very small drop) shown in **Fig. 16a**. Similar findings were also reported in Refs. [51, 79].

The variation of the calculated fibre bridging strength along with the composite crack strength for each section is presented in **Fig. 16d**. Like the distribution of the composite crack strength displayed in **Fig. 5b**, the fibre bridging strength followed a non-unform distribution, which agrees well with the real situation. When the nominal pore size in a given region exceeds a particular threshold, the weakening effect of lower local fibre dosage (i.e., reduction in fibre number) on fibre-bridging stress overwhelms the strengthening effect of increased effective interfacial frictional bond strength, as indicated in Eq. (14). As a result, this region tends to be more prone to cracking. As seen in **Fig. 5a**, the fibre number plays a dominant role in determining the fibre bridging strength as the changing trends are consistent with the fibre volume fraction based on the assumed value of γ in this study. However, in some cases, it is interesting to find that the sections with lower crack strength have higher fibre bridging stress, indicating that the final failure section would not be the section with lower crack strength. In comparison with the fibre bridging stress, the crack strength distribution depends on the combined effect of various factors including fibre dosage and crack size.

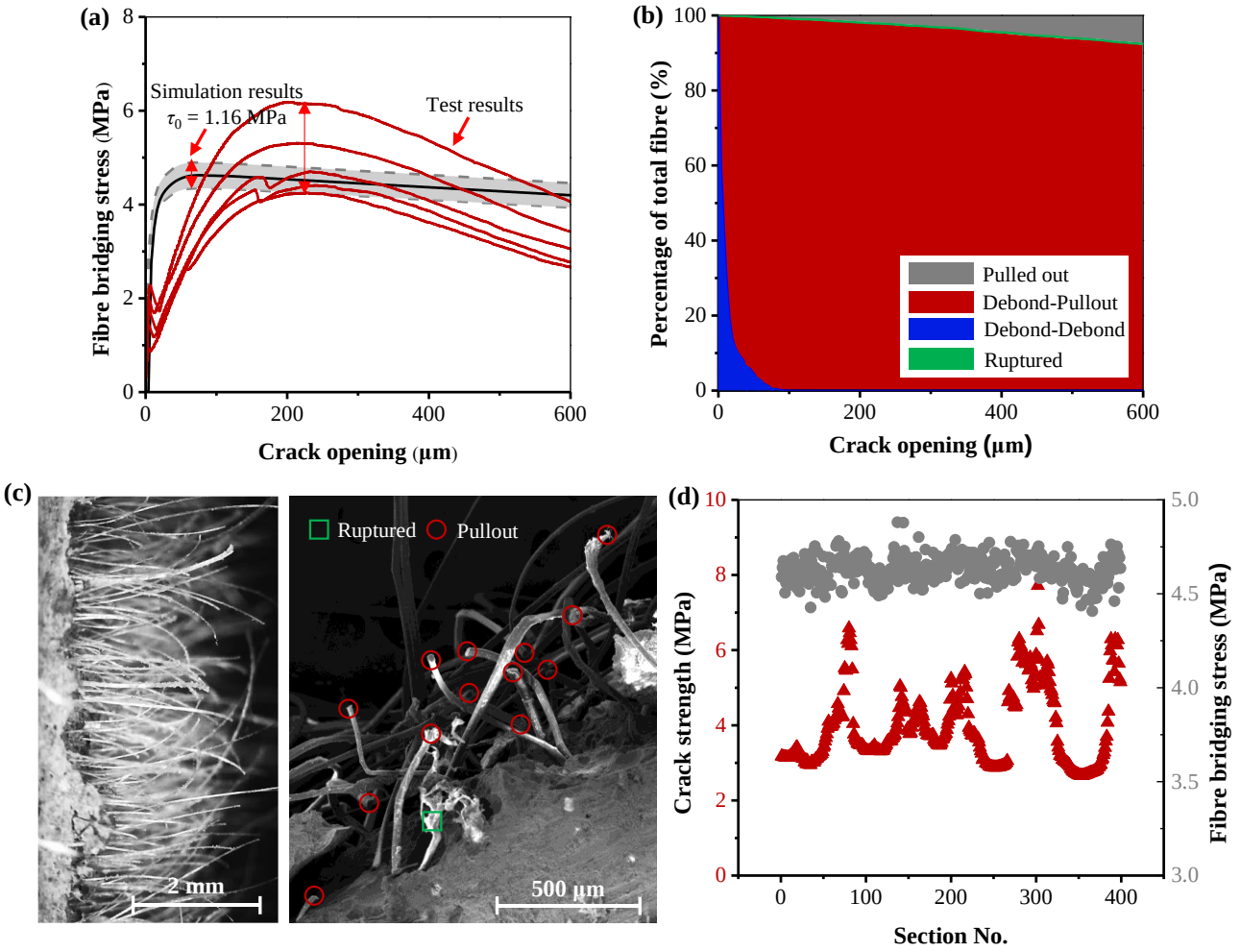

Fig. 16. (a) Measured and predicted σ-δ curves for PE-ECC, (b) percentage of fibres with different statuses under the same crack opening, (c) typical digital and SEM images with PE fibres across the fracture surface, and (d) distribution of fibre bridging strength and composite crack strength.

4.2 Comparison between predictions and experimental results of uniaxial tensile behaviour

To further verify the feasibility of using the proposed model to predict the multiple-cracking behaviour of ECC, uniaxial tension tests on typical dumbbell PE-ECC specimens with 2% fibre dosage and 30 mm thickness were conducted to obtain the stress-strain response. For experimental work, a normal-strength ECC with average 28-day compressive strength of 49.17 MPa (obtained from 60 × 60 × 60 mm cubes) was selected for validation. The test set-up and other details can be found in Ref. [57]. During the loading process, the deformation of the central part with 80 mm in length was measured using two external linear variable displacement transducers (LVDTs). The same plane size of the sample central part was adopted for numerical simulations. The tensile load was applied to samples at a constant loading rate of 0.5 mm/min according to the JSCE specification [69].

The stress-strain curve of the specimen under direct tension can be determined following the flow chart given in **Fig. 10** in combination with the input micromechanical parameters obtained in **Section 3**. Note that the elastic deformation between the cracks was ignored as the elastic deformation is insignificant compared to the crack opening displacement and the elastic modulus of the composite

does not remain constant throughout the tensile process, making it difficult to run real-time measurements. The tensile strain at a given stress was obtained by dividing the sum of the corresponding opening displacements of all cracks by the gauge region length (80 mm). After reaching the ultimate tensile stress, further loading would lead to the formation of a single major crack where the sample deformation would localise at the cracked section with the maximum crack opening. To indicate the slip softening characteristics of PE-ECC, 90% of the peak stress at the final failure section was further applied as the end point of the load step.

Both the predicted and experimental results in terms of stress-strain curves are plotted in **Fig. 17**. The experimental data show a large scatter of the tensile properties for mould-cast PE-ECC with greater thickness, including ultimate tensile strength (σ_{tu}) of 4.79 ± 0.25 MPa, ultimate tensile strain capacity (ε_{tu}) of 4.77 ± 1.85%, and number of cracks (Nc) of 46 ± 9. The predicted data of tensile properties in terms of first crack strength (2.64 ± 0.02 MPa), ultimate tensile strength (4.35 ± 0.27 MPa) and ultimate tensile strain capacity (5.22 ± 1.59%) are in good agreement with experimental data. To illustrate the general situation, 10 Monte Carlo simulations were first performed with the mean alue of the initial interfacial frictional bond strength (i.e., 1.16 MPa), and the 3 stress-strain curves corresponding to the maximum, minimum and mean values of the predicted minimum cross-section fibre bridging stress (which governs the ultimate tensile strength) are shown as black curves (predictions 1, 2 and 3) in **Fig. 17a**. Similar to the results of the single crack tests, the prediction results are found to exhibit a small scatter when the initial frictional bond strength is fixed. The average tensile strain capacity of the 3 predicted curves are close to that of the test results, indicating a reasonable prediction. The relatively smaller scatters of predictions compared to the measured results (i.e., test-1, test-2, test-3 and test-4) can be explained by the fact that for Monte Carlo simulations the position (z), diameter (d_f), and fibres orientation (θ) were set as random numbers while the value of τ_0 was kept constant. For instance, a smaller variation of the predicted ultimate tensile strength implies that the fibre location (i.e., embedment length), orientation and diameter have only a slight influence on the ultimate tensile strength. Then, different initial bond frictional strengths (τ_0 = 1 and 1.23 MPa) were adopted to obtain new prediction results (i.e., prediction-4 and prediction-5) to compare with the corresponding test results with lowest and highest tensile strain capacity (i.e., test-2 and test-4) in **Fig. 17a**. It can be indicated that the variation of the predicted tensile ductility of PE-ECC is primarily ascribed to fluctuations in interfacial frictional bond strength, followed by fibre location, orientation and diameter, which is consistent with that presented in Ref. [44]. Note that unlike 3 curves for the case of τ_0 = 1.16 MPa, only one σ-δ curve for each case of τ_0 = 1 MPa and 1.23 MPa was presented for comparation. Here, 10 Monte Carlo simulations were performed to obtain the fibre bridging strength for different sections. Then, the case corresponding to the minimum predicted fibre bridging strength close to the average value of all lowest predicted fibre bridging strength was

selected for further multiple cracking process prediction. In addition, in order to make the prediction results of the fibre-bridging stress representative, the selected calculated minimum peak fibre-bridging stress (i.e., the minimum tensile strength) among all cross-sections was close to the average value after 10 Monte Carlo simulations. **Fig. 17b** shows typical cracking patterns of PE-ECC corresponding to the case of test-3. Uneven distribution of crack locations and crack widths can be found, which will be further discussed in the next subsection combined with the preidicted results.

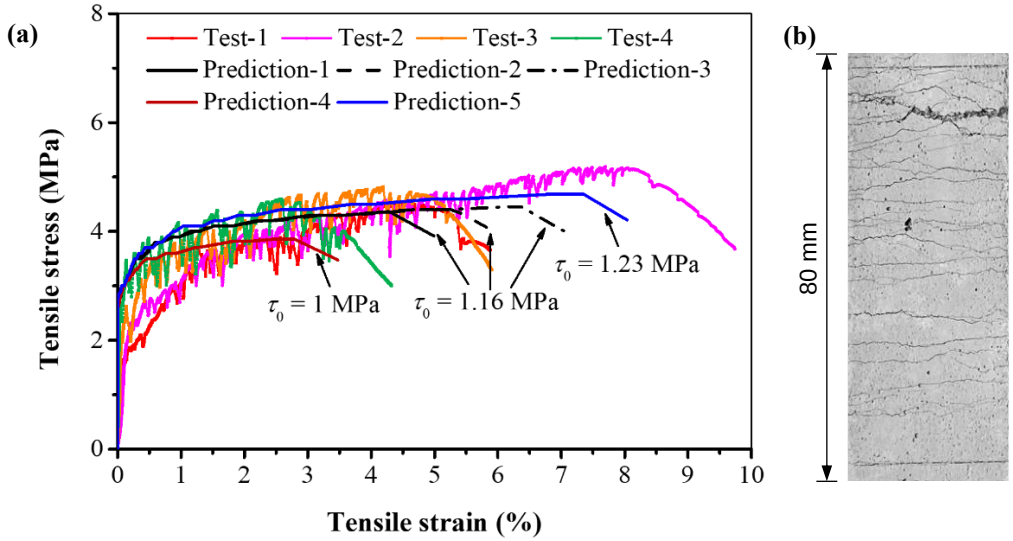

Fig. 17. (a) Comparison between experimental and predicted tensile stress-strain curves for PE-ECC; (b) typical cracking patterns of PE-ECC.

Fig. 18 demonstrates the three typical predictions of sequential formation of multiple cracking and the crack opening distribution on all cracked sections at the ultimate tensile stress, indicating that the predicted crack location and width are randomly distributed along the specimens. Hence, the analytical model proposed in this study can appropriately predict the sequential generation of multiple cracks. Dense cracks at three locations can be observed, which agrees well with the actual phenomenon and can be associated with the distribution of nominal local fibre volume fraction (equivalent to nominal local pore size distribution) shown in **Fig. 5a**. In **Fig.18**, the crack opening distributions of all cracked sections under the ultimate tensile strength for different cases were also presented. The larger the crack width, the bigger the data dots drawn. The calculated crack strength of all sections was the same for these three cases and the first composite crack strength occurred at the same section (No. 354) with the lowest value of 2.65 MPa. Due to the random input parameters of position, orientation and diameter of the fibres, the predicted stress-strain curves for these cases varied with the final failure of sections of No. 353, No. 366, and No. 349, respectively. A significant difference can be observed between the predictions and experimental findings in terms of number of cracked sections for the sample with tensile ductility of 4.61% (N_c = 48). The number of cracks obtained from prediction-1, prediction-2, and prediction-3 was found to be 122, 129, and 137, respectively, which were 2.7 times (prediction-2) that obtained from experiments. This can be

attributed to the number of sections divided and the macroscopic cracks formed from a combination of several microcracks. Besides, all cracked sections inside the specimen may not be detected by the visual inspection. The predicted crack widths were all controlled within 100 μm and the average crack width was 32.94 μm. at the ultimate strain (see **Fig. 19**), which is crucial for the durability of ECC. The opening displacement of most cracked sections was in the range of 20-40 μm.

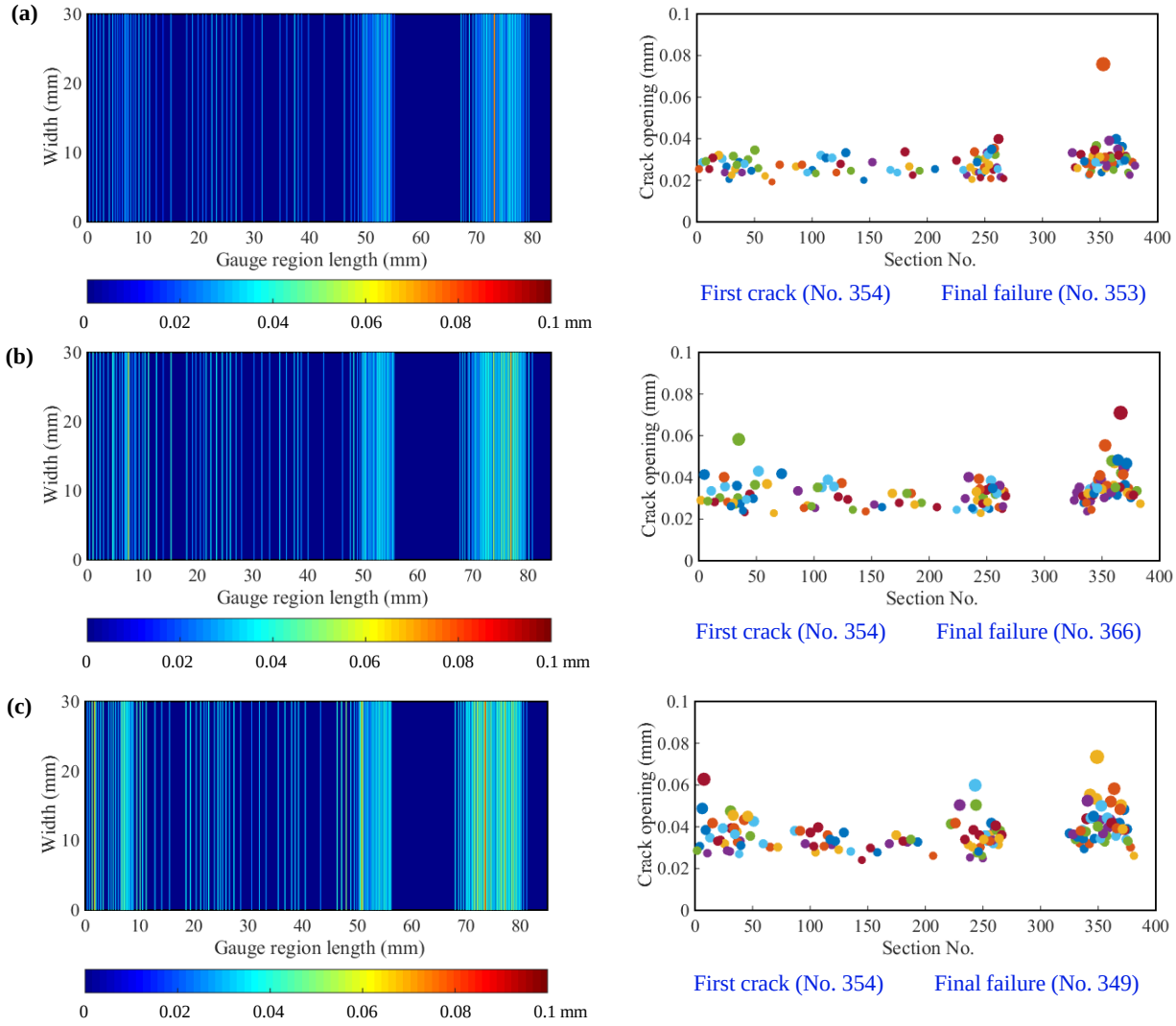

Fig. 18. Predictions of multiple cracking distribution at the ultimate tensile strength for (a) prediction-1, (b) prediction-2 and (c) prediction-3.

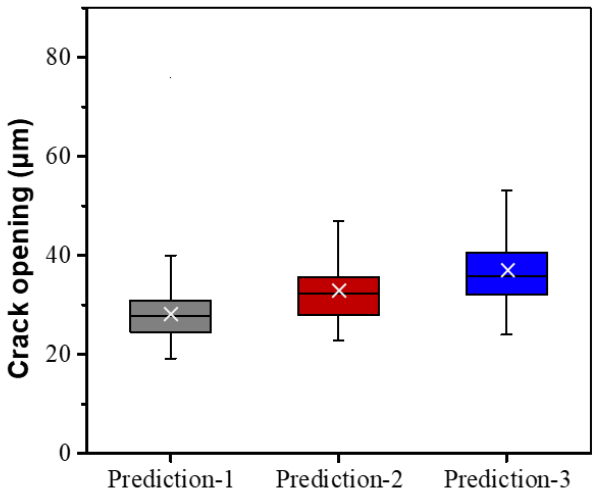

Fig. 19. Predicted crack width distribution of prediction-1, prediction-2, and prediction-3.

5. Parametric study

In this section, a parametric study was carried out to estimate the effects of three crucial parameters related to fibre-matrix interfacial properties including interfacial frictional bond strength reduction factor (γ), fibre length (l_f) and fibre orientation distribution ($p(\theta)$) on tensile stress-strain relationship and crack width distribution of PE-ECC. The results obtained from prediction-2 shown in **Fig. 17** were regarded as the reference to illustrate the effect of each parameter. As described in Section 4, 10 Monte Carlo simulations to determine the fibre bridging stress for each case were also performed. The calculated minimum peak fibre-bridging stress (i.e., the minimum tensile strength) among all cross-sections closest to the average value after 10 simulations was selected for futher multiple cracking process prediction with the constant initial bond strength of 1.16 MPa.

5.1 Effect of interfacial frictional bond strength reduction factor

Fig. 20 shows the effects of interfacial frictional bond strength reduction factor (γ = 19, 21 and 23) on the relationship between the newly defined factor (ξ_n) and local fibre volume fraction for the n^{th} section (V_{fn}) and the typical tensile stress-strain curves of PE-ECC obtained from predictions. It can be found that both the ultimate tensile strength and ductility decreased with the increase of γ. The ultimate tensile strength for γ = 19, 21, and 23 was 4.70, 4.41 and 4.12 MPa, respectively, while the ultimate tensile ductility was 7.45%, 5.30% and 3.64%, respectively, suggesting that the tensile ductility was more dependent on γ compared to tensile strength. According to Eqs. (13) and (14), a smaller γ would lead to a less reduction of interfacial frictional bond strength (see **Fig. 20a**), and thus a higher effective interfacial frictional bond strength. Additionally, while the frictional bond strength is assumed to vary linearity with local fibre friction in this work, a non-linear relationship between ξ_n and V_{fn} (as illustrated in **Fig. 20a**) is also possible and this will be a topic for future study.

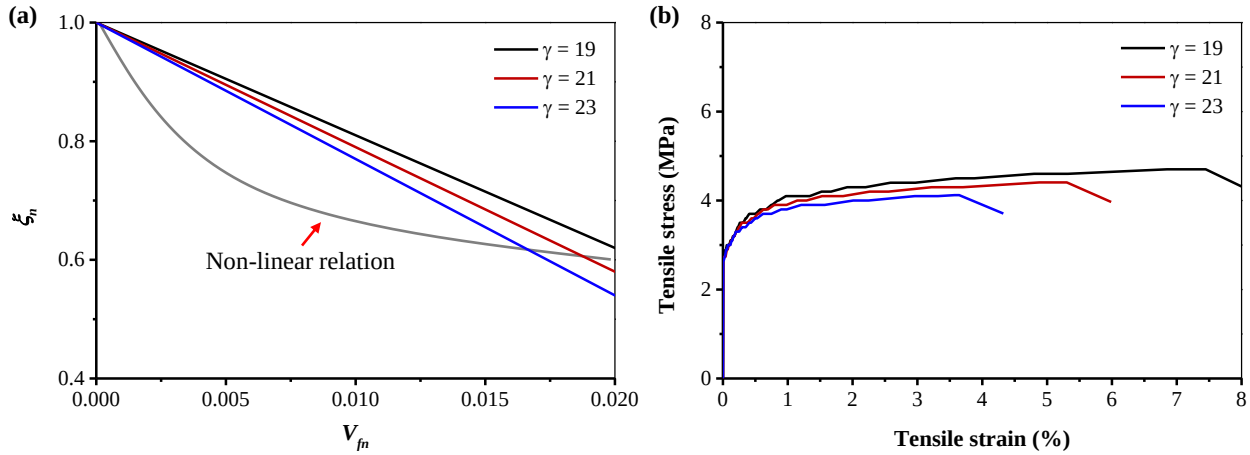

Fig. 20. (a) ξ_n against local fibre volume fraction for the n^{th} section (V_{fn}), and (b) typical tensile stress-strain curves of PE-ECC predicted accounting for various interfacial frictional bond strength reduction factors (γ = 19, 21 and 23).

Figs. 21 and **22** illustrate the effect of γ on the sequential formation of multiple cracking and crack width distribution under the peak fibre-bridging strength for ECC specimens. As γ increased, the average crack width dropped, while the difference was not significant. The crack opening for γ = 19, 21 and 23 was 35.1 ± 8.2 μm, 32.9 ± 7.2 μm and 31.7 ± 6.6 μm, respectively. The number of cracks was greatly reduced from 170 to 92, which agrees well with the changing trend of ductility. It is worth noting that the frictional bond strength should not be too high for a given strength grade of ECC, e.g., the one studied here with an average 28-day compressive strength of 49.17 MPa. Considering a single variable, if the interfacial frictional bond strength exceeds the critical value, there would exist an increased risk of fibre rupture during the debonding process. In fact, excessively high bond strength (e.g., over 2 MPa that is common for high-strength PE-ECC) is unrealistic for the normal-strength ECC in this study. If the bond is indeed so high, other characteristics, e.g., composite crack strength, would change, resulting in the prediction results depending on a more complex multiple effect.

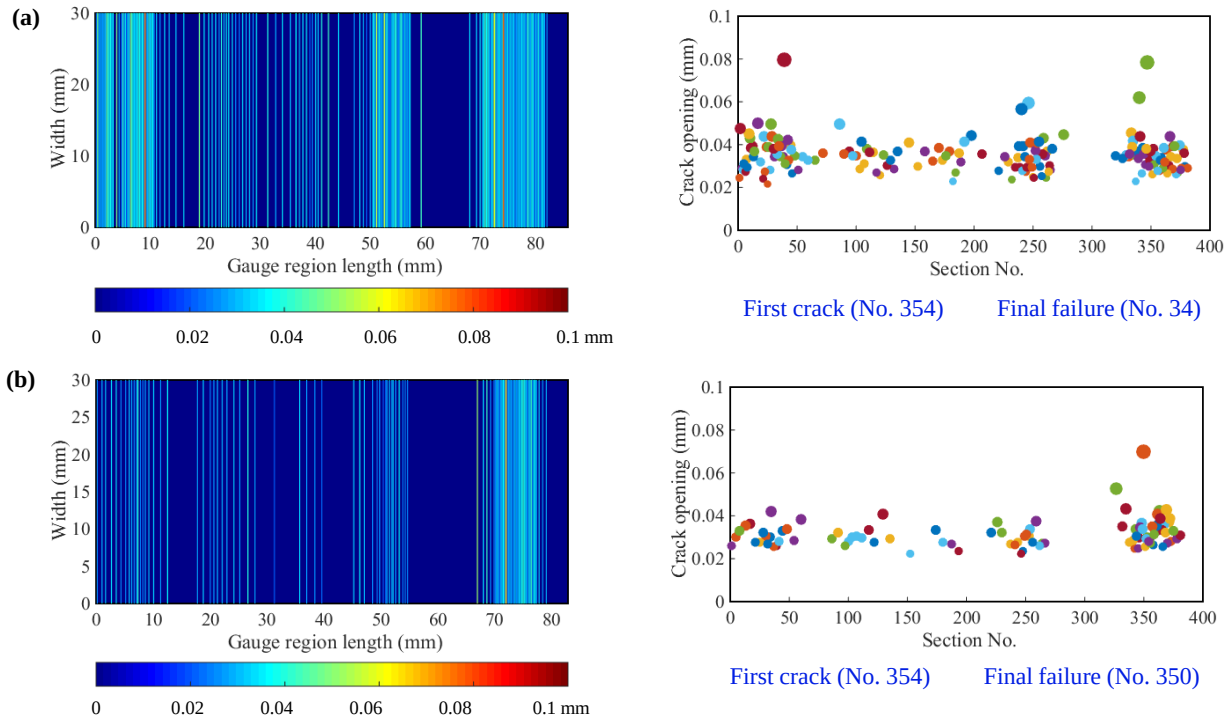

Fig. 21. Predicted multiple cracking features for (a) γ = 19 at the ultimate tensile strength of 4.70 MPa; (b) γ = 23 at the ultimate tensile strength of 4.12 MPa.

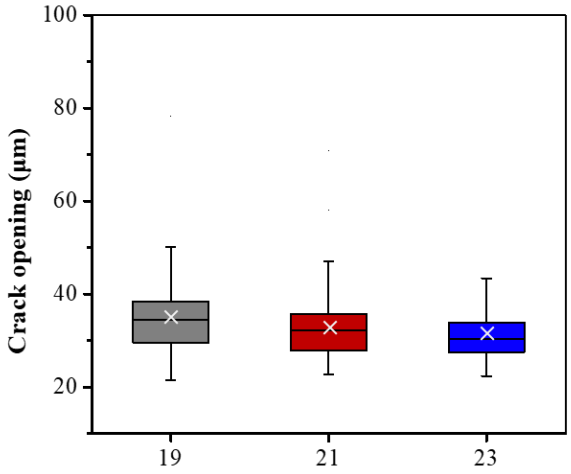

Fig. 22. Predicted crack width distribution in ECC specimens considering γ = 19, 21, and 23.

5.2 Effect of fibre length

Fig. 23 presents the representative tensile stress-strain curves of PE-ECC predicted for different fibre lengths, where the same 2% fibre content was adopted for all three cases. Specifically, 6 mm and 12 mm denote the 2% PE fibres with a constant length of 6 mm and 12 mm, respectively. The 2% fibres with 6 mm (1.5%) and 12 mm (0.5%) PE fibres is denoted as 6 + 12 mm. It can be observed that both the ultimate tensile strength and ductility increased with the increase of the fibre length. The ultimate tensile strength for the cases of 6 mm, 6 + 12 mm, and 12 mm was 3.58 MPa, 4.41 MPa and 7.06 MPa, respectively, while the ductility was 0.77%, 5.30%, and 18.26%, respectively, indicating that long fibres would be beneficial to both the ultimate tensile strength and ductility. This can be

explained by the fact that the longer fibre can provide a longer embedment length and generate a higher fibre bridging stress as the maximum embedment length is half of the fibre length. On the other hand, longer fibres are prone to rupture with the increasing applied load and crack opening, which typically occur for PVA fibres, whereas such risk can be negligible for normal-strength PE-ECC due to the high strength and elastic modulus of the fibre, as well as the moderate bond strength. As such, both the ultimate tensile strength and ductility continue to rise with the increase of fibre length.

As per the existing literature [80, 81], the average tensile ductility of 12 mm PE fibre reinforced ECC with a similar compressive strength grade was found to be 6.18 ± 0.5% and 9.78 ± 1.17%, respectively, with a maximum tensile ductility of 10.86%. The authors's previous work [57] indicated that the average tensile ductility of similar strength ECC reinforced respectively with 12 mm and 6 mm PE fibres was 7.31 ± 1.83% (with a maximum tensile ductility of 10.14%) and 2.45 ± 0.42%, respectively. All these suggest that the predictions in this study overestimated the tensile ductility for PE-ECC with 100% 12 mm fibre and underestimated that for PE-ECC with 100% 6 mm fibre. The main reason is that longer fibres may bring more air into the matrix during the mixing process, leading to higher porosity (greater probability of the occurrence of large pores) and lower effective interfacial frictional bond strength (according to Eq. (11)), and thus affect the bridging stress-strain relationship at the crack plane. Hence, the initial interfacial frictional bond strength should be selected in the upper interval of the test results (i.e., ranging from 1.16 to 1.46 MPa) for 6 mm PE-ECC and in the lower interval of the test results (i.e., ranging from 0.86 to 1.16 MPa) for 12 mm PE-ECC. From a different perspective, changing the fibre parameters may also alter the microstructural characteristics of the matrix, e.g., fibre number and interfacial frictional bond strength. Therefore, if considering the variations of different fibre parameters, the specimen's microstructural features need to be reset for a more accurate prediction.

Figs. 24 and **25** demonstrate the effect of fibre length (l_f) on the sequential formation of multiple cracking and crack width distribution under the peak fibre-bridging strength. It can be found that the average crack width went up with the increase of l_f with a large difference, suggesting that the fibre length had a significant influence on the tensile ductility of PE-ECC. The crack opening for l_f = 6 mm, 6 + 12 mm, and 12 mm was 13.4 ± 2.5 μm , 32.9 ± 7.2 μm and 44.8 ± 5.8 μm, respectively. In addition, the number of cracks was significantly increased from 46 to 326, which is consistent with the change in tensile ductility.

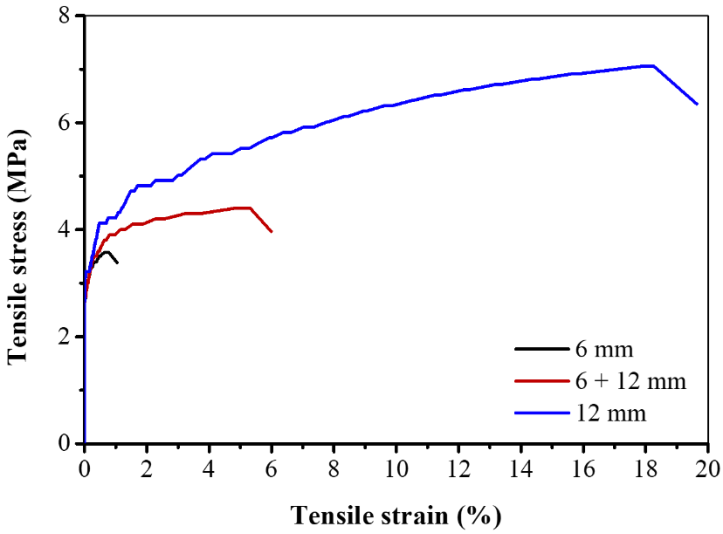

Fig. 23. Typical tensile stress-strain curves of PE-ECC predicted considering different fibre lengths.

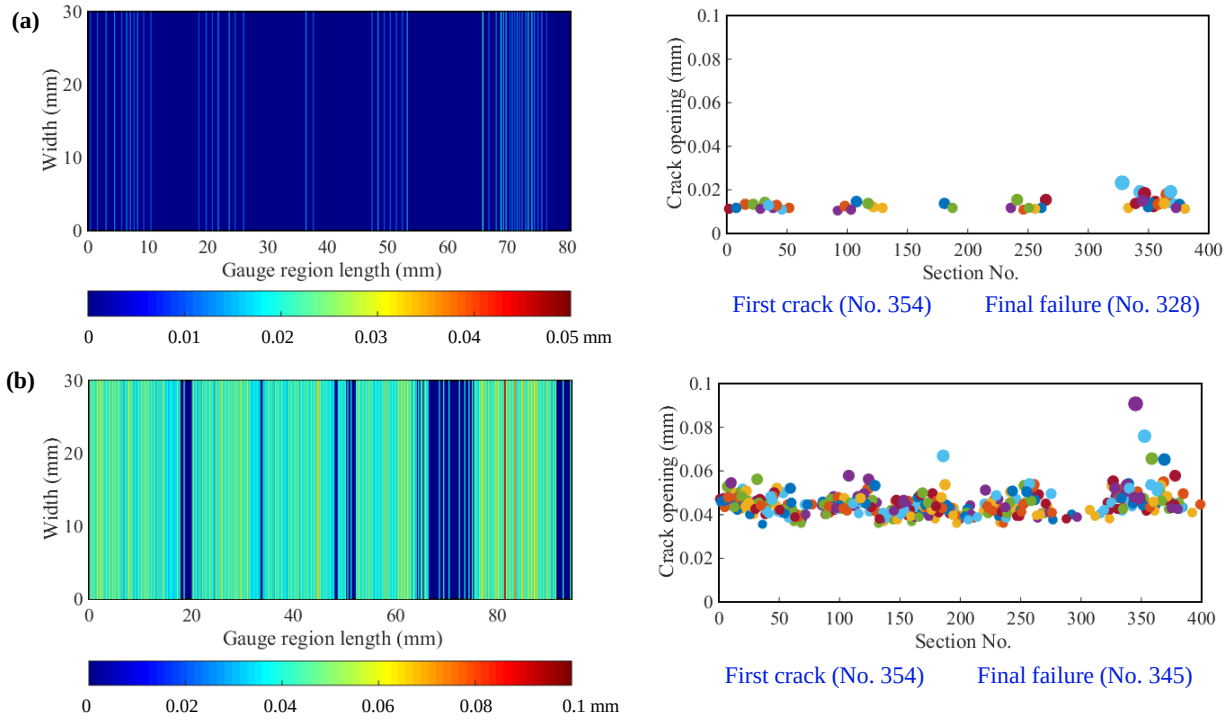

Fig. 24. Predicted multiple cracking features for (a) l_f= 6 mm at the ultimate tensile strength of 3.58 MPa; (b) l_f= 12 mm at the ultimate tensile strength of 7.06 MPa.

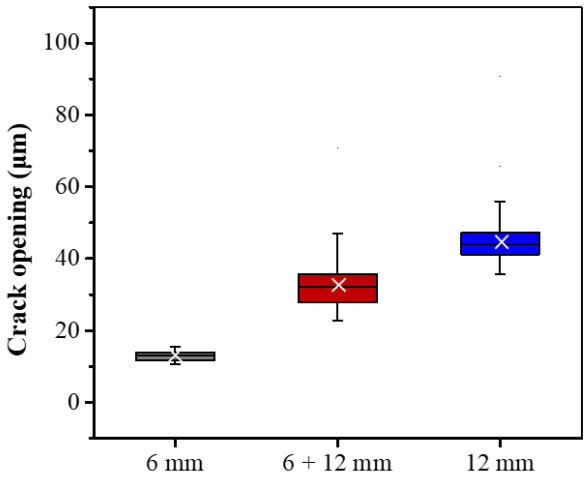

Fig. 25. Predicted crack width distribution of l_f = 6 mm, 6 + 12 mm, and 12 mm.

5.3 Effect of fibre orientation

Fig. 26 displays the fibre orientation distribution in terms of r and q and typical tensile stress-strain curves of PE-ECC predicted for three different cases. The ultimate tensile strength decreased with the increase of fibre inclination from 4.78 MPa to 3.39 MPa. The ECC specimens with smaller fibre orientations have a greater effective number of fibres bridging the crack surface. However, due to the snubbing effect and the apparent fibre strength reduction effect, fibres with a very large inclination for the case of r = 7 and q = 1.8 are more prone to rupture prematurely during the pull-out process and will no longer contribute to the fibre bridging action in ECC. Regarding the tensile strain capacity, it can be found that the tensile ductility increased first and then decreased with the increasing fibre inclination. A comparable tensile ductility can be observed for specimens with fibre orientation parameters (r, q) of (7, 1.8) and (3, 5.8), which agrees well with the finding reported in Ref. [82].

Figs. 27 and **28** show the sequential formation of multiple cracking and crack width distribution under the peak fibre-bridging strength. Similar to the tensile ductility, the average crack width that governs the tensile strain capacity of ECC went up first and then dropped with the increasing fibre inclination. The crack opening for the fibre orientation parameters (r, q) of (7, 1.8), (5, 3.8), and (3, 5.8) was 31.2 ± 7.1 μm, 32.9 ± 7.2 μm and 37.3 ± 7.9 μm, respectively, and the number of cracks for them was 72, 129 and 71, respectively. These can be ascribed to the stress transfer distance (x_d). For the case of (7, 1.8), due to the relatively low fibre bridging stress, the number of sections with crack strength smaller than the bridging stress would be reduced and the force (i.e., the pulley force shown in **Fig. 9a**) transferred into the matrix would also be lower. The stress transfer distance (x_d) and fibre bridging strength (σ_b) as a function of crack opening (δ) for PE-ECC specimnes with matrix strength σ_{mu} = 3 MPa and V_f = 0.02 (1.5 vol% 6 mm and 0.5 vol% 12 mm fibres) and different fibre orientations are presented in **Fig. 29**. By comparing the crack spacing calculated at the ultimate tensile strength, the lowest crack spacing occurred for the case of (5, 3.8) while the crack spacing for the cases of (3, 5.8) and (7, 1.8) was similar and relatively large.

Recently, ECC has been successfully designed with acceptable printability for extrusion-based 3D concrete printing, the tensile capacity of which is highly dependent on fibre orientation. The printed ECC was found to have higher tensile ductility than normal mould-cast ECC due to a higher fibre alignment in the printing direction as well as the reduction of the single factor of the fibre inclination. As the increase of interfacial frictional bond strength can effectively reduce the stress transfer distance, a proper fibre alignment combined with a relatively large interfacial frictional bond strength can be adopted to gain a desirable tensile behaviour of ECC [45].

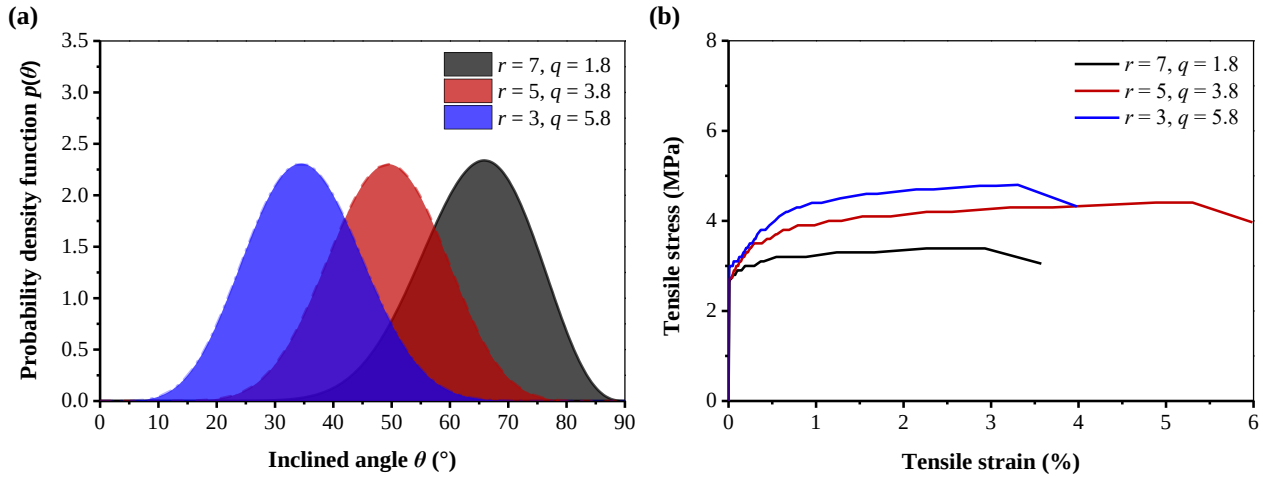

Fig. 26. (a) Different fibre orientation distribution; (b) predicted typical tensile stress-strain curves of PE-ECC considering different fibre orientations.

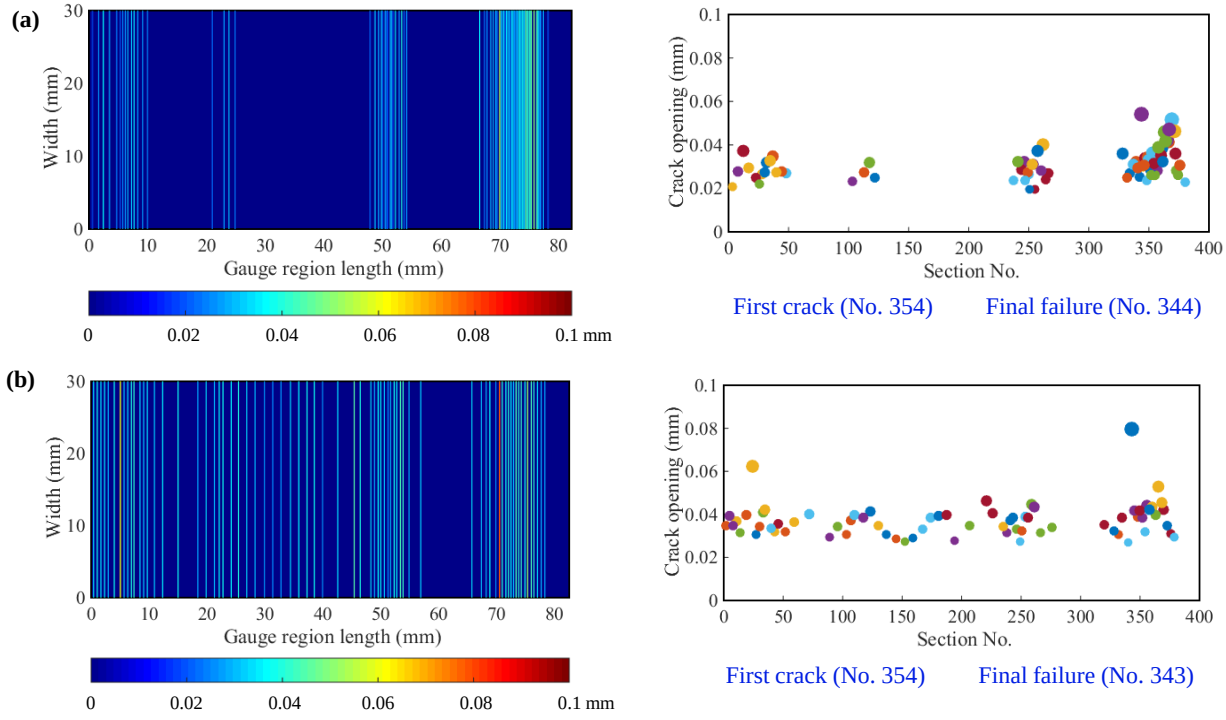

Fig. 27. Predicted multiple cracking features for fibre orientation distribution of (a) $r = 7$, $q = 1.8$ at the ultimate tensile strength of 3.39 MPa; (b) $r = 3$, $q = 5.8$ at the ultimate tensile strength of 4.78 MPa.

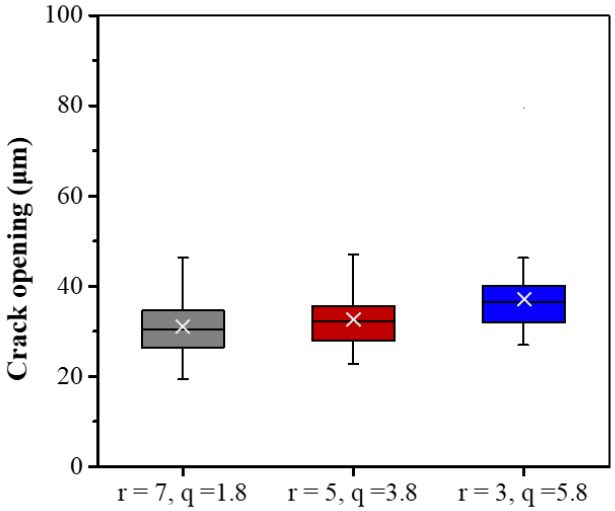

Fig. 28. Predicted crack width distribution for fibre orientation parameters (r, q) of (7, 1.8), (3, 5.8), and (3, 5.8).

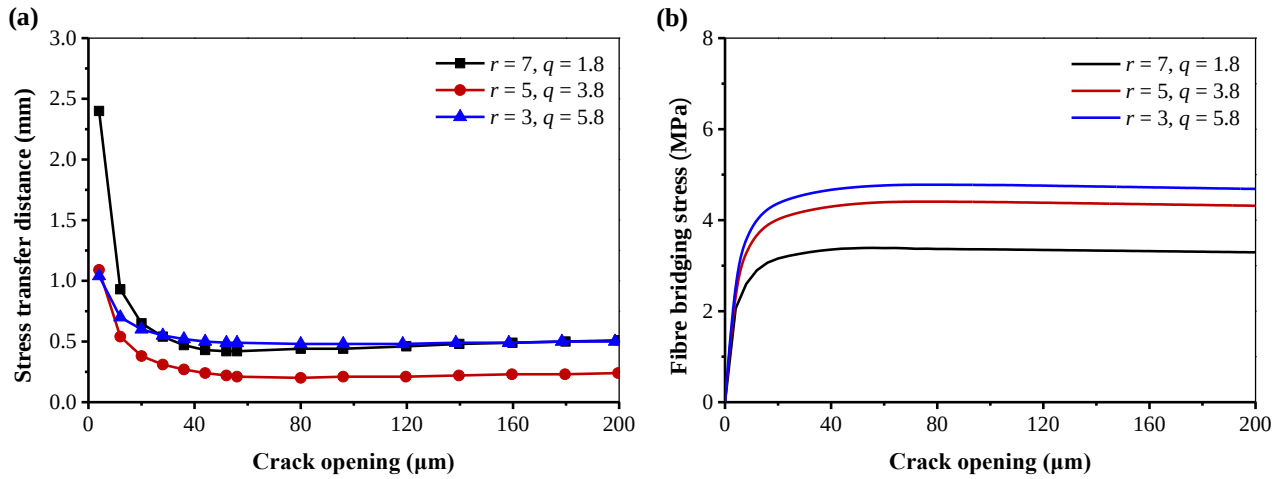

Fig. 29. (a) Stress transfer distance (x_d) against crack opening (δ) with tensile stress of matrix of σ_{mu} = 3 MPa and fibre volume fraction of V_f = 0.02 and (b) fibre bridging stress (σ_b) against δ (1.5% 6 mm and 0.5% 12 mm fibres) for different fibre orientations.

6. Conclusions

In this study, a practical micromechanical analytical model accounting for the pore structure characteristics and fibre-matrix interaction was proposed to predict the tensile properties of PE-ECC, with a special focus on strain-hardening and multiple microcracking behaviour. A series of Monte Carlo simulations were conducted to predict the single crack tensile and tensile behaviour of PE-ECC, which was validated with experimental data. This was followed by a systematic parametric study to assess the effects of crucial parameters on tensile properties. Based on the predictions and experimental results, the main conclusions can be drawn as follows:

(1) Direct tensile test on the notched plain ECC specimens can be used to determine the matrix toughness of ECC based on the relationship between crack strength and measured pore size. The fibre-matrix interface properties can be properly obtained from single fibre pull-out tests using the developed setup. For a PE-ECC, the initial interfacial frictional bond strength is found to be 1.16 ±

0.3 MPa and the average slip-hardening parameter is 0.004 ± 0.00028. All the aligned fibres exhibited the pull-out failure mode but retained the slight slip hardening behaviour. The microstructural characteristics of PE-ECC obtained from X-ray computed tomography and backscattered electron imaging along with image processing also served as an important basis for the accurate prediction of tensile behaviour of PE-ECC.

(2) The new factor (ξ_n) and interfacial frictional bond strength reduction factor (γ) proposed in this study facilitate the calculations of composite crack strength and fibre bridging strength. The good agreement between the predicted crack-bridging relationships and experimental results suggests that the developed model can provide a reliable prediction of tensile properties of PE-ECC, including cracking sequence and tensile stress-strain curves. The interfacial frictional bond strength played a dominant role in the predicted tensile ductility of PE-ECC, followed by fibre location, orientation and diameter.

(3) The parametric study indicated that a higher interfacial frictional bond strength reduction factor (γ) led to smaller ultimate tensile strength (σ_{tu}) and tensile ductility (ε_{tu}) within a certain range and the interfacial frictional bond strength (τ) showed a more significant effect on ε_{tu} than σ_{tu}; Both σ_{tu} and ε_{tu} went up with the increase of fibre length from 6 mm to 12 mm. σ_{tu} dropped with the increase of fibre inclination, while ε_{tu} increased initially and then reduced with the increasing fibre inclination due to the change in stress transfer distance. Thus, the ranges of input parameter values should be controlled within the limits for a certain compressive strength level of PE-ECC to achieve desirable properties in terms of ultimate strength, ultimate strain, and average crack width.

The prediction accuracy can be further improved by considering more microstructural characteristics and micromechanical parameters. For instance, the influences of various pore size distribution and non-uniform fibre distribution induced by different manufacturing processes can be considered to develop a novel framework for modelling the processing-microstructure-properties relation of ECC reinforced with different types of fibre.

Acknowledgements

This study was funded by the National Natural Science Foundation of China (No. 52130210), Victoria-Jiangsu Innovation and Technology R&D Fund (BZ2020019), and China Scholarship Council (No.202006090274). M. Zhang gratefully acknowledges the financial support from the Engineering and Physical Sciences Research Council (EPSRC), UK under Grant No. EP/R041504/1 and the Royal Society, UK under Award No. IEC\NSFC\191417.

References

[1] V.C. Li, High-performance and multifunctional cement-based composite material, Engineering, 5(2) (2019) 250-260.

[2] V.C. Li, Engineered Cementitious Composites (ECC): Bendable Concrete for Sustainable and

Resilient Infrastructure. 2019: Springer.

[3] V.C. Li, H.C. Wu, Conditions for pseudo strain-hardening in fiber reinforced brittle matrix composites, Appl. Mech. Rev., 45(8) (1992) 390-398.

[4] D. Zhang, J. Yu, H. Wu, B. Jaworska, B.R. Ellis, V.C. Li, Discontinuous micro-fibers as intrinsic reinforcement for ductile engineered cementitious composites (ECC), Compos. B Eng., 184 (2020) 107741.

[5] D. Y. Yoo, N. Banthia, High-performance strain-hardening cementitious composites with tensile strain capacity exceeding 4%: A review, Cement Concr. Compos., 125 (2022) 104325.

[6] J.X. Zhu, L.Y. Xu, B.T. Huang, K.F. Weng, J.G. Dai, Recent developments in Engineered/Strain-Hardening Cementitious Composites (ECC/SHCC) with high and ultra-high strength, Constr. Build. Mater., 342 (2022) 127956.

[7] Y. Ding, K.Q. Yu, M. Li, A review on high-strength engineered cementitious composites (HS-ECC): Design, mechanical property and structural application, Structures, 35 (2022) 903-921.

[8] L. Wang, N.U. Rehman, I. Curosu, Z. Zhu, M.A.B. Beigh, M. Liebscher, V. Mechtcherine, On the use of limestone calcined clay cement (LC3) in high-strength strain-hardening cement-based composites (HS-SHCC), Cement Concr. Res., 144 (2021) 106421.

[9] L.Y. Xu, B.T. Huang, V.C. Li, J.G. Dai, High-strength high-ductility Engineered/Strain-Hardening Cementitious Composites (ECC/SHCC) incorporating geopolymer fine aggregates, Cement Concr. Compos., 125 (2022) 104296.

[10] B.T. Huang, J. Yu, J.Q. Wu, J.G. Dai, C.K. Leung, Seawater sea-sand Engineered Cementitious Composites (SS-ECC) for marine and coastal applications, Compos. Commun., 20 (2020) 100353.

[11] S.C. Figueiredo, C.R. Rodríguez, Z.Y. Ahmed, D.H. Bos, Y. Xu, T.M. Salet, O. Çopuroğlu, E. Schlangen, F.P. Bos, Mechanical behavior of printed strain hardening cementitious composites, Materials, 13 (10) (2020) 2253.

[12] K. Yu, W. McGee, T.Y. Ng, H. Zhu, V.C. Li, 3D-printable engineered cementitious composites (3DP-ECC): fresh and hardened properties, Cement Concr. Res., 143 (2021) 106388.

[13] S. Chaves Figueiredo, C. Romero Rodríguez, Z.Y. Ahmed, D.H. Bos, Y. Xu, T.M. Salet, O. Çopuroğlu, E. Schlangen, F.P. Bos, An approach to develop printable strain hardening cementitious composites, Mater. Des., 169 (2019) 107651.

[14] J. Ye, C. Cui, J. Yu, K. Yu, J. Xiao, Fresh and anisotropic-mechanical properties of 3D printable ultra-high ductile concrete with crumb rubber, Compos. B Eng., 211 (2021) 108639.

[15] B. Zhu, J. Pan, B. Nematollahi, Z. Zhou, Y. Zhang, J. Sanjayan, Development of 3D printable engineered cementitious composites with ultra-high tensile ductility for digital construction, Mater. Design., 181 (2019) 108088.

[16] B.T. Huang, Y.T. Wang, J.Q. Wu, J. Yu, J.G. Dai, C.K. Leung, Effect of fiber content on mechanical performance and cracking characteristics of ultra-high-performance seawater sea-sand concrete (UHP-SSC), Adv. Struct. Eng., 24 (6) (2021) 1182-1195.

[17] B.T. Huang, J.Q. Wu, J. Yu, J.G. Dai, C.K.Y. Leung. High-strength seawater sea-sand engineered cementitious composites (SS-ECC): mechanical performance and probabilistic modelling, Cement Concr. Compos., 114 (2020) 103740.

[18] S. Zhang, V.C. Li, G. Ye, Micromechanics-guided development of a slag/fly ash-based strain-hardening geopolymer composite, Cement Concr. Compos., 109 (2020) 103510.

[19] H. Zhong, M. Zhang, Effect of recycled tyre polymer fibre on engineering properties of sustainable strain hardening geopolymer composites, Cement Concr. Compos., 122 (2021) 104167.

[20] B. Nematollahi, J. Sanjayan, F.U.A. Shaikh, Comparative deflection hardening behavior of short fiber reinforced geopolymer composites, Constr. Build. Mater., 70 (2014) 54-64.

[21] H.H. Nguyễn, Q.H. Lương, J.I. Choi, R. Ranade, V.C. Li, B.Y. Lee, Ultra-ductile behavior of fly ash-based engineered geopolymer composites with a tensile strain capacity up to 13.7%, Cement Concr. Compos., (2021) 104133.

[22] K. Yu, H.e. Zhu, M. Hou, V.C. Li, Self-healing of PE-fiber reinforced lightweight high-strength engineered cementitious composite, Cement Concr. Compos., 123 (2021) 104209.

[23] S.Z. Qian, J. Zhou, M.R. de Rooij, E. Schlangen, G. Ye, K. van Breugel, Self-healing behavior of strain hardening cementitious composites incorporating local waste materials, Cement Concr. Comp., 31 (2009) 613-621.

[24] P. Zhang, Y. Dai, X. Ding, C. Zhou, X. Xue, T. Zhao, Self-healing behaviour of multiple microcracks of strain hardening cementitious composites (SHCC), Constr. Build. Mater., 169 (2018) 705-715.

[25] H. Zhu, D. Zhang, T. Wang, V.C. Li, Intrinsic self-stressing and low carbon engineered cementitious composites (ECC) for improved sustainability, Cement Concr. Res., 149 (2021) 106580.

[26] H. Zhu, D. Zhang, Y.C. Wang, T.Y. Wang, V.C. Li, Development of self-stressing engineered cementitious composites (ECC), Cement Concr. Compos., 118 (2021) 103936.

[27] V. Corinaldesi, A. Nardinocchi, Mechanical characterization of Engineered Cement-based Composites prepared with hybrid fibres and expansive agent, Compos. B Eng., 98 (2016) 389-396.

[28] Z. Zhang, Q. Zhang, V.C. Li, Multiple-scale investigations on self-healing induced mechanical property recovery of ECC, Cement Concr. Compos., 103 (2019) 293-302.

[29] A. Spagnoli, A micromechanical lattice model to describe the fracture. behaviour of engineered

cementitious composites, Comp. Mater. Sci., 46(1) (2009) 7-14.

[30] M. Luković, H. Dong, B. Šavija, E. Schlangen, G. Ye, K. van Breugel, Tailoring strain-hardening cementitious composite repair systems through numerical experimentation, Cement Concr. Compos., 53 (2014) 200-213.

[31] J. Kang, J. E. Bolander, Multiscale modeling of strain-hardening cementitious composites. Mech. Res. Commun., 78 (2016) 47-54.

[32] T. Huang, Y.X. Zhang, C. Yang, Multiscale modelling of multiple-cracking tensile fracture behaviour of engineered cementitious composites, Eng. Fract. Mech., 160 (2016) 52-66.

[33] C. Chen, H. Cai, J. Li, P. Zhong, B. Huang, L. Sui, Y. Zhou, One-Dimensional extended FEM based approach for predicting the tensile behavior of SHCC-FRP composites, Eng. Fract. Mech., 225 (2020) 106775.

[34] T. Shi, C.K.Y. Leung, An effective discrete model for strain hardening cementitious composites: model and concept, Comput. Struct., 185 (2017) 27-46.

[35] V.C. Li, H.C. Wu, Conditions for pseudo strain-hardening in fiber reinforced brittle matrix composites, Appl. Mech. Rev., 45 (1992) 390-398.

[36] V.C. Li, C.K.Y. Leung, Steady-state and multiple cracking of short random fiber composites, J. Eng. Mech., 118 (1992) 2246-2264.

[37] T. Kanda, V.C. Li, Effect of fiber strength and fiber-matrix interface on crack bridging in cement composites, J. Eng. Mech., 125 (1999) 290-299.

[38] V.C. Li, C. Wu, S. Wang, A. Ogawa, T. Saito, Interface tailoring for strain-hardening polyvinyl alcohol-engineered cementitious composite (PVA-ECC), ACI Mater. J., 99 (2002) 463-472.

[39] V.C. Li, S. Wang, Microstructure variability and macroscopic composite properties of high performance fiber reinforced cementitious composites, Probab. Eng. Mech., 21 (2006) 201-206.

[40] E.H. Yang, S. Wang, Y. Yang, V.C. Li, Fiber-bridging constitutive law of engineered cementitious composites, J. Adv. Concr. Technol., 6 (2008) 181-193.

[41] R. Ranade, V.C. Li, M.D. Stults, T.S. Rushing, J. Roth, W.F. Heard, Micromechanics of High-Strength, High-Ductility Concrete, ACI Mater. J., 110 (4) 375-384.

[42] C. Lu, C.K.Y. Leung, A new model for the cracking process and tensile ductility of strain hardening cementitious composites (SHCC), Cement Concr. Res., 79 (2016) 353-365.

[43] C. Lu, C.K. Leung, V.C. Li, Numerical model on the stress field and multiple cracking behavior of engineered cementitious composites (ECC), Constr. Build. Mater., 133 (2017) 118-127.

[44] J. Li, J. Weng, E.H. Yang, Stochastic model of tensile behavior of strain-hardening cementitious composites (SHCCs), Cement Concr. Res., 124 (2019) 105856.

[45] J. Li, J. Weng, Z. Chen, E.H. Yang, A generic model to determine crack spacing of short and randomly oriented polymeric fiber-reinforced strain-hardening cementitious composites

(SHCC), Cement Concr. Compos., 118 (2021) 103919.

[46] V.C. Li, Y.J. Wang, S. Backer, A micromechanical model of tension-softening and bridging toughening of short random fiber reinforced brittle matrix composites, J. Mech. Phys. Solids., 39(5) (1991) 607-625.

[47] J. Li, E.H. Yang, Probabilistic-based assessment for tensile strain-hardening potential of fiber-reinforced cementitious composites, Cement Concr. Compos., 91 (2018) 108-117.

[48] E. Grande, G. Milani, Numerical simulation of the tensile behavior of FRCM strengthening systems, Compos. B Eng., 189 (2020) 107886.

[49] M. Vořechovský, R. Rypl, R. Chudoba, Probabilistic crack bridge model reflecting random bond properties and elastic matrix deformation, Compos. B Eng., 139 (2018) 130-145.

[50] R. Chudoba, Y. Li, R. Rypl, H. Spartali, M. Vořechovský, Probabilistic multiple cracking model of brittle-matrix composite based on a one-by-one crack tracing algorithm, Appl. Math. Model., 92 (2021) 315-332.

[51] B.T. Huang, J.Q. Wu, J. Yu, J.G. Dai, C.K. Leung, V.C. Li, Seawater sea-sand engineered/strain-hardening cementitious composites (ECC/SHCC): assessment and modeling of crack characteristics, Cement Concr. Res., 140 (2021) 106292.

[52] H.C. Wu, V.C. Li, Snubbing and bundling effects on multiple crack spacing of discontinuous random fiber‐reinforced brittle matrix composites, J. Am. Ceram. Soc., 75(12) (1992) 3487-3489.

[53] V.C. Li, S.X. Wang, Microstructure variability and macroscopic composite properties of high performance fiber reinforced cementitious composites, Probab. Eng. Mech., 21(3) (2006) 201-206.

[54] G.A. Rao, Long-term drying shrinkage of mortar- influence of silica fume and size of fine aggregate, Cement Concr. Res., 31 (2001) 171-175.

[55] I.M. Nikbin, M.H.A. Beygi, M.T. Kazemi, J.V. Amiri, E. Rahmani, S. Rabbanifar, M. Eslami, Effect of coarse aggregate volume on fracture behavior of self compacting concrete, Constr. Build. Mater., 52 (2014) 137-145.

[56] C.K. Leung, V.C. Li, First-cracking strength of short fiber-reinforced ceramics, Ceram. Eng. Sci. Proc., (1989) 1164-1178.

[57] B.R. Zhu, J.L. Pan, J.R. Li, P.H. Wang, M.Z. Zhang, Relationship between microstructure and strain-hardening behaviour of 3D printed engineered cementitious composites, Cement Concr. Compos., (2022) in press.

[58] C. Lu, V.C. Li, C.K.Y. Leung, Flaw characterization and correlation with cracking strength in Engineered Cementitious Composites (ECC), Cement Concr. Res., 107 (2018) 64-67.

[59] C.K. Leung, N. Ybanez, Pullout of inclined flexible fiber in cementitious composite, J. Eng.

Mech., 123(3) (1997) 239-46.

[60] J. Yu, J. Yao, X. Lin, H. Li, J.Y.K. Lam, C.K.Y. Leung, I.M.L. Sham, K. Shih, Tensile performance of sustainable Strain-Hardening Cementitious Composites with hybrid PVA and recycled PET fibers, Cement Concr. Res., 107 (2018) 110-123.

[61] Z. Lin, V.C. Li, Crack bridging in fiber reinforced cementitious composites with slip-hardening interfaces, J. Mech. Phys. Solids., 45 (1997) 763-787.

[62] J. Morton, G.W. Groves, The effect of metal wires on the fracture of a brittle-matrix composite, J. Mater. Sci., 11(4) (1976) 617-622.

[63] T. Kanda, V.C. Li, Interface property and apparent strength of high-strength hydropholic fiber in cement matrix, J. Mater. Civ. Eng., 10 (1) (1998) 5-13.

[64] M. Xia, H. Hamada, Z. Maekawa, Flexural stiffness of injection molded glass fibre reinforced thermoplastics, Int. Polym. Process., 10 (1995) 74-81.

[65] ASTM E 399-12, Standard Test Method for Linear-Elastic Plane-Strain Fracture Toughness KIc of Metallic Materials, ASTM International, West Conshohocken, PA, 2014.

[66] RILEM FMC-50, Determination of the fracture energy of mortar and concrete by means of three-point bend tests on notched beams, 18 (4) (1985) 287-290.

[67] T.L. Anderson, Fracture mechanics: fundamentals and applications, CRC press, 2017.

[68] JC/T 2641-2018. Standard test method for the mechanical properties of ductile fibre reinforced cementitious composites, Beijing, China Building Materials Press, 2018.

[69] JSCE, Recommendations for Design and Construction of High Performance Fibre Reinforced Cement Composites with Multiple Fine Cracks, Japan Society of Civil Engineers, Tokyo, Japan, 2008, 1-16.

[70] ASTM, C 469 Standard Test Method for Static Modulus of Elasticity and Poisson's Ratio of Concrete in Compression, 2010.

[71] D.Y. Lei, L.P. Guo, Y. Li, J.P. Liu, B. Chen, D.X. Li, S.C. Li, V. Mechtcherine, Micro-mechanical model for ultra-high strength and ultra-high ductility cementitious composites (UHS-UHDCC), Constr. Build. Mater., 267 (2021) 120668.

[72] Z. Lin, T. Kanda, V.C. Li, On interface property characterization and performance of fiber reinforced cementitious composites, Concr. Sci. Eng., 1 (1999) 173-174.

[73] 1998, TR 49 Design guidance for high strength concrete (includes amendment No. 3, May 2013 (incorporating amendments 1 and 2)).

[74] J.D. Wu, L.P. Guo, Y.Z. Cao, B.C. Lyu, Mechanical and fiber/matrix interfacial behavior of ultra-high-strength and high-ductility cementitious composites incorporating waste glass powder, Cement Concr. Compos., 126 (2022) 104371.

[75] Y.Z. Li, J.X. Li, E.H. Yang, X.C. Guan, Investigation of matrix cracking properties of engineered

cementitious composites (ECCs) incorporating river sands, Cement Concr. Compos., 123 (2021) 104204.

[76] J.X. Li, E.H. Yang, Probabilistic-based assessment for tensile strain-hardening potential of fiber-reinforced cementitious composites, Cement Concr. Compos., 91 (2018) 108-117.

[77] C. Lu, J. Yu, C.K. Leung, An improved image processing method for assessing multiple cracking development in Strain Hardening Cementitious Composites (SHCC), Cement Concr. Compos., 74 (2016) 191-200.

[78] Y. Wang, F. Liu, J. Yu, F. Dong, J. Ye, Effect of polyethylene fiber content on physical and mechanical properties of engineered cementitious composites, Constr. Build. Mater., 251 (2020) 118917.

[79] I. Curosu, E. Muja, M. Ismailov, A. H. Ahmed, M. Liebscher, V. Mechtcherine, An experimental-analytical scale-linking study on the crack-bridging mechanisms in different types of SHCC in dependence on fiber orientation, Cement Concr. Res., 152 (2022) 106650.

[80] L. Li, Z. Cai, K. Yu, Y.X. Zhang, Y. Ding, Performance-based design of all-grade strain hardening cementitious composites with compressive strengths from 40 MPa to 120 MPa, Cement Concr. Compos., 97 (2019) 202-217.

[81] J. Ye, C. Cui, J. Yu, K. Yu, F. YDong, Effect of polyethylene fiber content on workability and mechanical-anisotropic properties of 3D printed ultra-high ductile concrete, Constr. Build. Mater., 281 (2021) 122586.

[82] W.H. Liu, L.W. Zhang, K.M. Liew, A cyclic plastic-damage multiphase model for evaluation of multiple cracking in strain hardening cementitious composites, J. Mech. Phys. Solid., 158 (2022) 104692.